Infrared Spectroscopy of Gadolinium

by

Laila Obied

B.Sc., Misrata University, Misrata-Libya, 2003

A THESIS SUBMITTED IN PARTIAL FULFILMENT OF
THE REQUIREMENTS FOR THE DEGREE OF

MASTER OF SCIENCE

in

The Faculty of Mathematics and Sciences

Department of Physics

BROCK UNIVERSITY

February 14, 2012

2011 © Laila Obied

Abstract

Measurements of the optical reflectivity of the normal incident light along c-axis [0001] have been made on a Gadolinium single crystal, for temperatures between 50 K and room temperature just above the Curie temperature of Gd, which is 293 K. And covering the spectrum range between 100 -11000 cm^{-1}. This work is the first study of Gd in the far infrared range. In fact it fills the gap below 0.2 eV which has never been measured before.

Extreme attention was paid to the fact that Gadolinium is a very reactive metal with air. Thus, the sample was mechanically polished and carefully handled during the measurement. However, temperature dependent optical measurements have been made in the same frequency range for a sample of Gd_2O_3. For comparison, both samples of Gd and Gd_2O_3 were examined by X-Ray diffraction. XRD analysis showed that the sample was pure gadolinium and the oxide layer either does not exist, or is very thin. Furthermore, this fact was supported by the absence of any of Gd_2O_3 features in the Gd sample reflectivity.

Kramers Kronig analysis was applied to extract the optical functions from the reflectance data. The optical conductivity shows a strong temperature dependence feature in the mid-infrared. This feature disappears completely at room temperature which supports a magnetic origin.

Contents

List of Tables

List of Figures

Acknowledgements

First and foremost I want to thank my supervisor, Professor David Crandles, for his guidance, continous encouragement and most appreciable his patience with my English language. He really has impacted my way of thinking physics.

I would like to thank the members of my committee, Dr. Kirill Samokhin and Dr. Thad A. Harroun, for their valuable discussion and helpful comments.

It is a pleasure to thank whole physics department, Faculty members and staff, for their kindness and welcoming spirit from the first time I came to the department.

I am indebted to many of my colleagues for sharing their lab experience and helping me whenever I needed their help.

The samples used in this work were examined by X-ray in McMaster University labs. I would like to thank Wen He Gong for doing the 2θ scans. And Antoni Dabkowski for Laue work.

I owe my deepest gratitude to the Sarwer family for taking care of my daughters and for being my second family.

Lastly, I would like to thank my family for all their love and encouragement. My parents who taught me that with hard work and determination almost anything is possible. And my husband, Ali, who I will be forever indebted to him for his endless patience and faithful support by all possible ways. I could have never done this without him.

Chapter 1

Introduction

Optical studies provides valuable information on the structure of electronic energy bands of rare earth metals (REM) and on the kinetic properties of carriers as well [1]. Gadolinium is one of the REM with interesting electronic and magnetic properties. The unique electronic and magnetic properties of this group of metals result from the coexistence of both highly localized and delocalized electron levels in the valence region [2]. The exchange coupling between the localized and delocalized magnetic moments of the electrons influences the transport effects and the optics of REM. To investigate these effects Gadolinium has been studied by different kinds of optical techniques on thin films, single crystal and polycrystalline samples.

The first motivation of this experimental work was to perform optical measurements in the FIR range of the spectra on Gadolinium single crystal which has never been studied. This will help investigating the low energy behaviour of the optical response functions.

There have been huge disagreements between previous optical measurements of Gd. Discussions of the reasons for this have focussed on the existence of an oxide layer which affects the optical constants. Gd is very reactive in air, so our second goal was to perform the optical measurements on Gd_2O_3, in case we needed to treat the Gd sample with a thin film of Gd_2O_3. Details about this part will be provided in a following chapter. The third goal was to investigate the temperature dependence of the optical response functions to understand the impact of the magnetic ordering

on ferromagnetic metals.

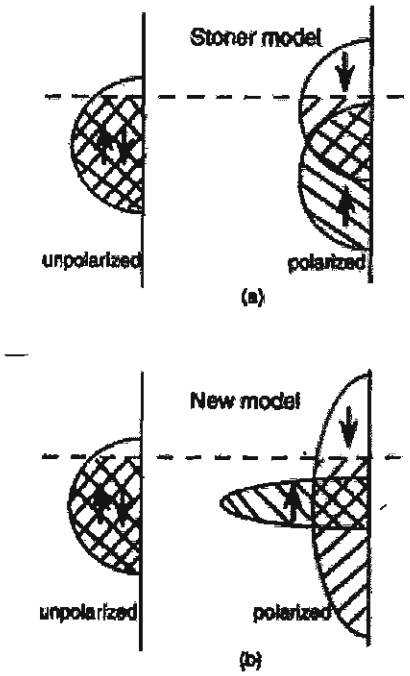

Figure 1.1: Density of states for spin up and down electrons in the unpolarized and magnetic states. The dashed line indicates the position of the Fermi level. In part b (Hirsch's model), for band filling above one half the broader band corresponds to minority spin carriers; for the band filling below one half, the situation is reversed [4].

The hope of this work mainly is to try to contribute towards understanding the origin of the metallic ferromagnetism. Back in 1938, Stoner [3] introduced his model to explain the metallic ferromagnetism based on a rigid shift that occurs between the majority and the minority spin bands. If $\epsilon_{k\downarrow}$ and $\epsilon_{k\uparrow}$ are the energies of the minority and majority spin electron bands, respectively, then the exchange splitting Δ can be given by :

$$\Delta = \epsilon_{k\downarrow} - \epsilon_{k\uparrow} \tag{1.1}$$

Hirsch [4] suggested a different mechanism to explain the origin of ferromagnetism.

In Hirsch model there is no overall shift in the energy of the majority and minority spin bands but there is a change in the bandwidth of the majority and minority spin electrons upon spin polarization [4]. Fig. 1.1 shows a scheme for the two models in terms of the density of states.

The model of Hirsch predicts a reduction of the effective mass of the charge carriers which leads to an increase in the kinetic energy upon the spin polarization. This mechanism should be seen in optical absorption data upon spin polarization as an increase in the plasma frequency ω_p ($\omega_p^2 \propto \frac{n}{m^*}$), where m^* is the effective mass and n the carrier concentration.

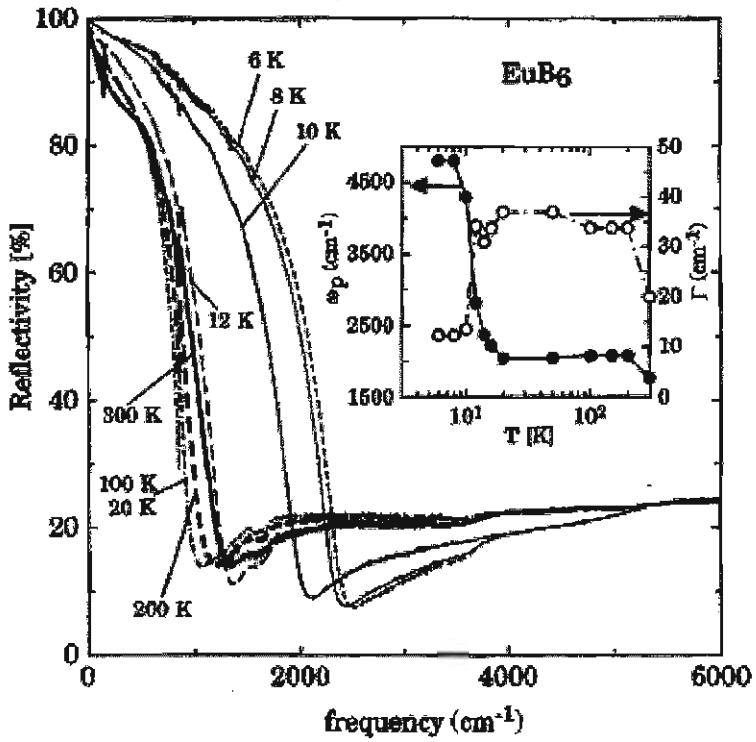

Figure 1.2: Reflectivity R(ω) of EuB_6 in the FIR and MIR spectral range at various temperatures between 6 and 300 K. The inset shows the plasma frequency $\omega_p(T)$ and the scattering rate $\Gamma(T)$ versus temperature[5].

Hirsch's model was supported by the data of EuB_6 which is a metallic ferromagnet with a Curie temperature (T_c) of 16K. L. Degiorgi et al. [5] have carried out reflectance measurements on this compound which showed that there was a shift in the plasma frequency as the temperature approaches the Curie temperature, as shown in Fig. 1.2. Also, the temperature dependence of the plasma frequency and the scattering rate (Γ) resulting from fitting the optical conductivity are shown in the inset of Fig. 1.2 [5].

Note that the plasma frequency increases sharply upon spin polarization. But there is almost no change above Curie temperature. Degiorgi et al. have explained this by either a reduction in the effective mass (in agreement with Hirsch model) or an increase in the concentration of the carriers or both together.

1.1 Material background

Gadolinium has hcp crystal structure with lattice constants a=b=3.636 Å and c=5.7826 Å with two atoms in the unit cell at $(\frac{1}{3}\frac{2}{3}\frac{1}{4})$ and $(\frac{2}{3}\frac{1}{3}\frac{3}{4})$. The atomic number is 64 , atomic weight 157.3, and density of 7.90×10^3 kg.m^{-3}. The basic electron configuration is $(4f^7 5d^1 6s^2)$. Gadolinium is unique for its special Curie temperature of 293 K [6]. Fig. 1.3 shows the primitive vectors for a simple hexagonal lattice.

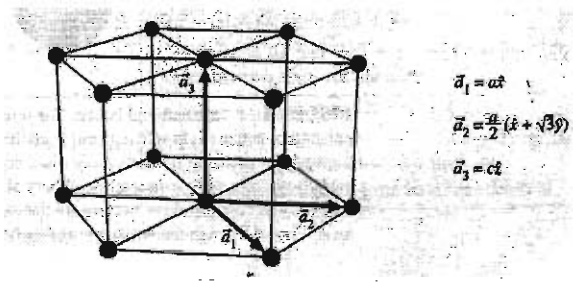

Figure 1.3: Primitive vectors for a simple hexagonal lattice [7].

1.1.1 Electrical Properties of Gadolinium

H. E. Nigh et al. [8] measured the electrical resistivity of a Gd single crystal along the b and c axes in the temperature range 4.2K - 380K. Fig(1.4) shows the experimental curve of the resistivity. Note that for the b-axis resistivity the slope changes at about 293.2 K. The c-axis resistivity exhibits a peak at about 293 K and becomes almost T-independent for the higher temperatures. Note that the residual resistivity is different for both directions. They have explained the behaviour of the c-axis resistivity above the Curie temperature to be due to the short range magnetic ordering which persists up to at least 340K [8].

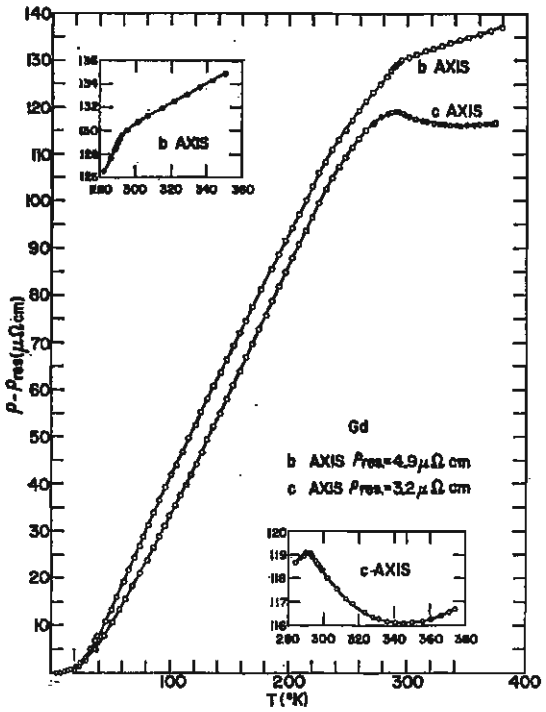

Figure 1.4: Electrical resistivity (ρ) of Gd single crystal for the b-axis and the c-axis versus temperature T [?]

Colven et al. [9] considered the electrical resistivity to be the sum of the residual resistivity (ρ_{res}), the magnetic contribution (ρ_{mag}), and the phonon contribution

(ρ_{ph}). They reported an estimated value of the magnetic contribution to the total electrical resistivity for T > T_c by extrapolating the linear high temperature part of the resistivity curve back to zero which means eliminating ρ_{ph} as follows:

$$\rho_{mag} = \rho - \rho_{ext} - \rho_{res} \approx 106.4(\Omega cm \times 10^{-6}) \tag{1.2}$$

where ρ_{ext} is the linear extrapolation of ρ above T_c to 0 K.

They also showed that the best fit of the experimental data to the electrical resistivity ρ_{poly} of a polycrystalline gadolinium is :

$$\rho_{poly} = \frac{1}{3}(2\rho_b + \rho_c) \tag{1.3}$$

where ρ_b and ρ_c are the b-axis and c-axis resistivities, respectively.

Studying the Hall effect sometimes allows the determination of the type and the number of charge carriers in the material. Gadolinium exhibts a very interesting Hall effect because of its magnetic properties [10]. In non-magnetic one-band materials the Hall effect can be described by the Hall coefficient R_o as follows:

$$R_o = \frac{E_y}{j_x B} = \frac{-1}{ne} \tag{1.4}$$

where E_y is the induced electric field in the material, j_x the current density, B the applied magnetic field, e the electron charge, and n the number of the current carriers per unit volume. But when non-zero magnetization is present in a material the Hall effect is described by considering the magnetization inside the sample in addition to the applied magnetic field :

$$e_H = R_o H + R_1 M \tag{1.5}$$

where e_H is the Hall electric field per unit current density, R_o the ordinary Hall coefficient (OHC), R_1 the extraordinary Hall coefficient (EHC), H the applied magnetic field, and M the magnetization.

Lee and Legvold have done a temperature dependent Hall effect study on Gd single crystal. Fig. 1.5 shows their measurement for the Ordinary Hall coefficient with the applied magnetic field along c-axis. They observed that the OHC changes sign at about 130 K and increases rapidly as the temperature increases. Lee and

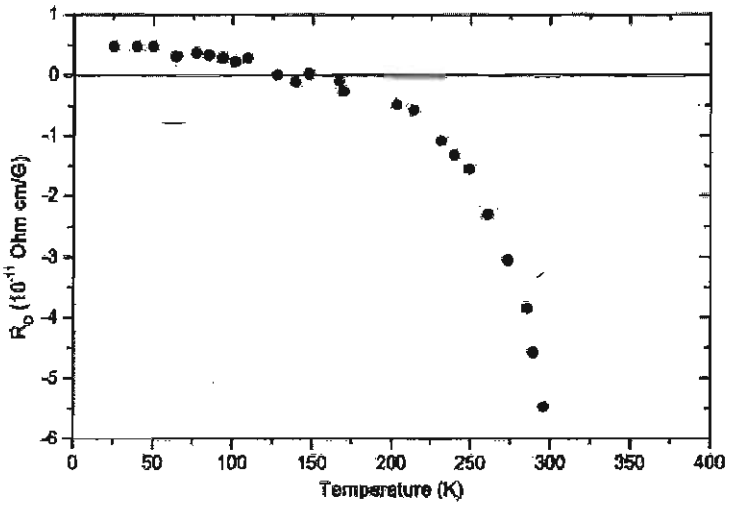

Figure 1.5: Gadolinium single crystal ordinary Hall coefficient R_0 vs temperature T [10]

Legvold [10] have suggested that the splitting of the conduction bands below Curie temperature could be responsible for the sharp increase and the sign change of R_0 [10]. Fig. 1.6 shows the Extraordinary Hall coefficient of Gd (R_1) versus temperature. As it is shown R_1 has strong temperature dependence, which rapidly decreases as T_c is approached because the magnetization decreases. However, S. A. Baily*et al.* [11] showed a different T dependence of the EHC and they explained that the discrepancy is due to the method of separating the OHC and EOH. Many theories suggest that R_1 is a consequence of the spin-orbit interaction. R_1 is predicted to be proportional to the square of the electrical resistivity [10].

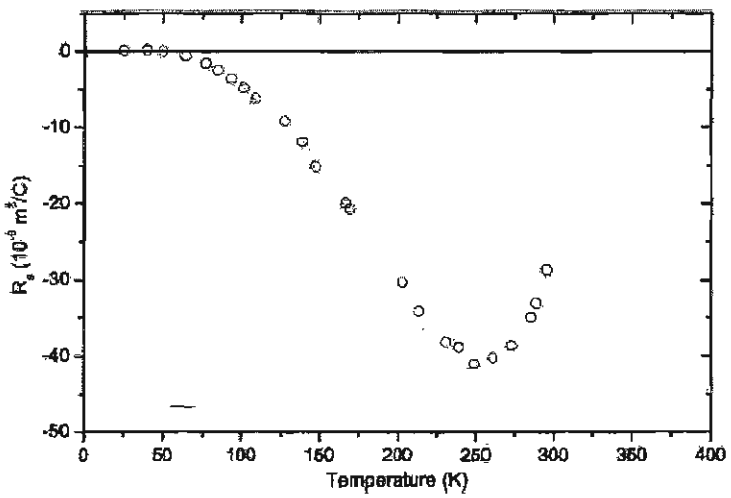

Figure 1.6: Gadolinium single crystal extraordinary Hall coefficient R_s (R_1) versus temperature T [10].

1.1.2 Magnetic Properties of Gadolinium

The magnetic properties of Gd in the ground state are well understood. The half filled 4f shell gives a total of spin angular momentum $S = \frac{7}{2}$ and orbital angular momentum $L = 0$, so $J = L + S = \frac{7}{2}$ [6]. The f electrons are localized moments and couple via RKKY type interaction (a long range interaction named after Ruderman, Kittel, Kasuya, and Yosida based on the exchange mechanism [12]) to a ferromagnetic Heisenberg-spin system [13].

The total magnetic moment per atom of Gd is 7.63 μ_B. 4f electrons contribute about $7\mu_B$ while the 0.63 μ_B comes from the polarization of the three electrons in the conduction band ($5d^16s^2$) by the exchange interaction with the 4f localized electrons [13] [14]. Fig. 1.7 shows the reduced spontaneous magnetization, which is the magnetization at zero applied magnetic field at a specefic temperature $\sigma_{0,T}$ devided by the magnetization at 0 K and zero applied magnetic field $\sigma_{0,0}$, of Gd along the b-axis versus temperature[8].

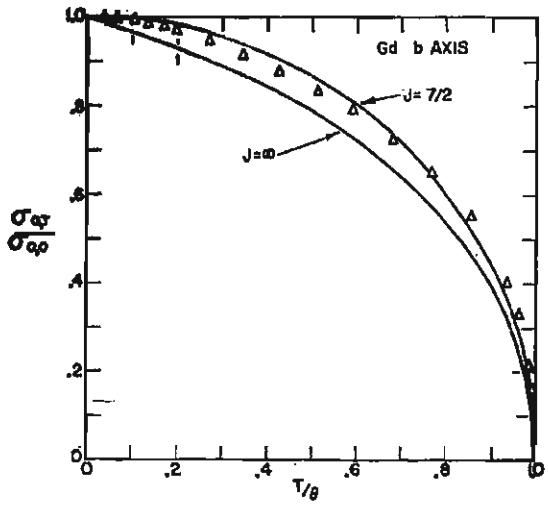

Figure 1.7: The reduced spontaneous magnetization $\frac{\sigma_{0,T}}{\sigma_{0,0}}$ curve of Gd versus temperature T. The solid lines are for the J=$\frac{7}{2}$ and J=∞ from the Weiss quantum theory of ferromagnetism. [8]

Through cooling down Gd shows magnetic ordering as it becomes a ferromagnetic. The localised moments of 4f shell are oriented parallel to the c crystallographic axis at temperatures 289 - 232 K. The angle between the magnetic moments and the c-axis increases below 232K and reaches the highest of 75° at 180K. Then it starts to decrease to a minimum of 32° at 4.2K [15].

The simple magnetic alignment of Gd is a result of having zero orbital angular momentum. Therefore Gd has relatively small magnetocrystalline anisotropy compared to the other rare earth metals.

A rare earth metal is considered to be composed of trivalent ions embedded in a sea of the conduction electrons [16]. In the heavy rare earths, and Gd is one of this series, the $4f$ shell is strongly bound (atomic like) and forms a very narrow energy band. The mean radius of this shell is one tenth of the interionic spacing. The overlap between the $4f$ orbitals from neighbouring ions is negligible. However,

there is a strong magnetic coupling between $4f$ orbitals. This coupling is the main producer of the magnetic ordering seen in these metals. This magnetic coupling is the consequence of the indirect exchange interaction mediated by the polarization of the conduction electrons. This interaction has an oscillatory nature and has a long range effect. The theory based in this mechanism is named after Ruderman, Kittel, Kasuya, and Yosida and is called the RKKY interaction [12]. This polarization $\sigma(r)$ is the conduction electrons at distance r from the localized spin S is given by :

$$\sigma(r) \propto SF(2k_f r) \tag{1.6}$$

k_f is the wave vector at the Fermi surface. The function $F(x)$ is given by:

$$F(x) = \frac{1}{x^4}(sinx - xcosx) \tag{1.7}$$

This function is a damped oscillation as shown in Fig 1.8. It causes an oscillatory variation of polarization of the spin of the conduction electrons. The exchange

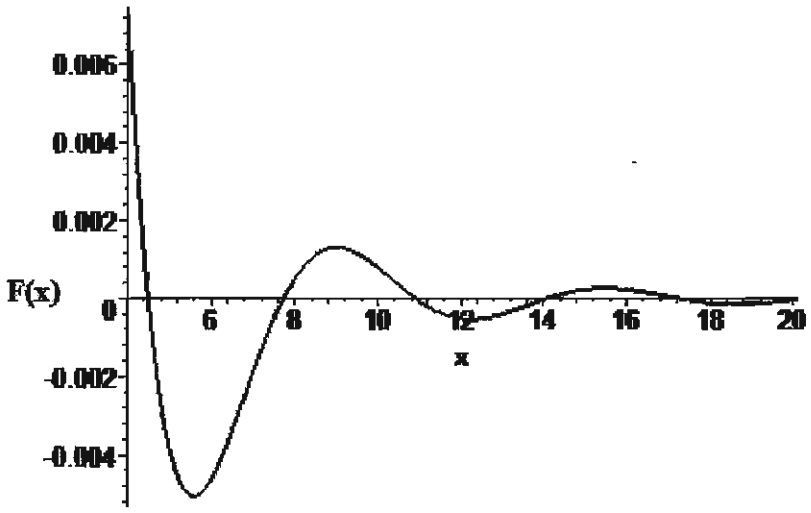

Figure 1.8: Functional form of RKKY interaction [12].

splitting of the conduction electrons in a heavy rare earth metals is given by:

$$\Delta E = 2JS \tag{1.8}$$

where J is an effective $s-f$ exchange energy and S is the spin of the rare earth ion [17]. An estimate of ΔE can be obtained for Gd from the calculated density of states at the Fermi surface and the observed saturation magnetization of $7.55\mu_B/atom$, that is $0.55\mu_B/atom$ more than is expected for an ion with $S = \frac{7}{2}$. The excess moment is assumed to arise from polarization of the conduction electrons through exchange interaction with the $4f$ electrons. If ΔE is the exchange splitting the excess moment $\Delta\mu$ is given by:

$$\Delta\mu = \frac{1}{4} g N(E_f) \Delta E \mu_B \tag{1.9}$$

where $N(E_f)$ is the total density of states at the Fermi energy and the g-factor refers to the conduction electrons. Using the value $N(E_f)$=1.8 electrons/atom eV calculated by Demmock [17] and assuming $g = 2$, we obtain $\Delta E = 0.61eV$ for Gd [17].

1.1.3 Electronic Band Structure of Gadolinium

The calculation of the energy bands can provide a good prediction of the optical response functions. The expected features in the optical conductivity and reflectivity data occur due to the interband and intraband transitions. The approximate energies of these transitions can be obtained from the energy band structure [18]. Fig. 1.9 shows the Brillouin zone of a simple hexagonal crystal.

J. O. Demmock *et al.* [17] have calculated the paramagnetic electronic band structure of Gd using the non-relativistic augmented plane wave (APW) method. They showed that the bands near the Fermi energy are mixed s-d character (Fig. 1.10). Also they reported that the $4f$ band is very narrow with a width of about 0.05 eV. This band lies below the bottom of the $5d$ - $6s$ bands by about 11 eV. Demmock

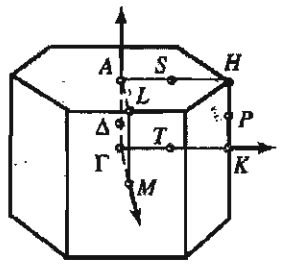

Figure 1.9: The standard labeling of the high symmetry points in the Brillouin zone of a simple haxagonal lattice [7].

has given an estimate of the exchange splitting of the *s-d* conduction band according to his resulting total density of states at the Fermi level to be 0.61 eV. While the experimental value of the position of 4 *f* bands reported by Lang *et al.* [19] is about 4.04 eV above the Fermi level for the minority 4*f* bands and 7.44 below Fermi level for the majority 4*f* bands. Therefore the splitting of the 4*f* bands is about 11.48 eV [19]. Lang *et al.* have obtained these values using X-ray photoelectron spectroscopy (XPS) for the occupied part and Bremsstrahlung isochromat spectroscopy (BIS) for the unoccupied part of the 4*f* bands. On the other hand, the most recent theoretical calculation of the band structure of Gd by Sapan *et al.* [20] using the Coulomb corrected Local Spin Density Approximation (LSDA + U), which includes the Coulomb parameter U and the exchange parameter J for the 4*f* electrons, gave the value of 8 eV below E_f for the majority *f* bands, and 3 eV above E_f for the minority *f* bands (see Fig. 1.11).

Their calculations shows that the width of the f bands is about 0.1 eV. Sapan [20] suggested that the spin up 4*f* states would not participate to the optical transitions in the low energy due to the energy well of 8 eV. It is to be noted from Fig.1.11 that the spin splitting of the conduction band is approximately 1.0 eV.

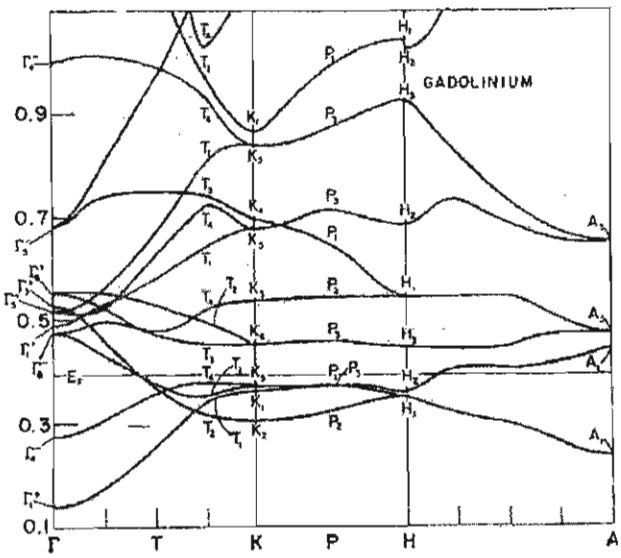

Figure 1.10: Calculated E(k) curves for the conduction band of Gd by Demmock *et al.* [17].

The detailed spin resolved band structure calculated by Nolting *et al.* [13] for Gd within the conduction band energy region is shown if Fig. 1.12. The method used was the Augmented Spherical Wave (ASW) band calculation. In their calculations they treated the $4f$ as a valence electrons and fully polarized. Fig. 1.12 shows the dispesionless spin up $4f$ subbands and spin down $4f$ subbands located at 4.5 eV below Fermi level and 0.5 eV above Fermi level, respectivily. The conduction bands ($6d$ - $5s$) are relatively broad and a k-independent spin-splitting of a ΔE about 1.0 eV. However, the spin-polarized augmented-plane-wave (APW) calculations by Harmon and Freeman [21] showed that the spin splitting of the conduction bands is not k-independent (Fig. 1.13). Note that 1 Ry=13.6 eV. Furthermore, the angle resolved photoemission study of the band structure by Dongqi *et al.* [22] showed that the exchange splitting of the conduction band is not uniform in the reciprocal space. This fact comes from the observation of that the temperature induced binding energy shift is not constant at different places in k-space.

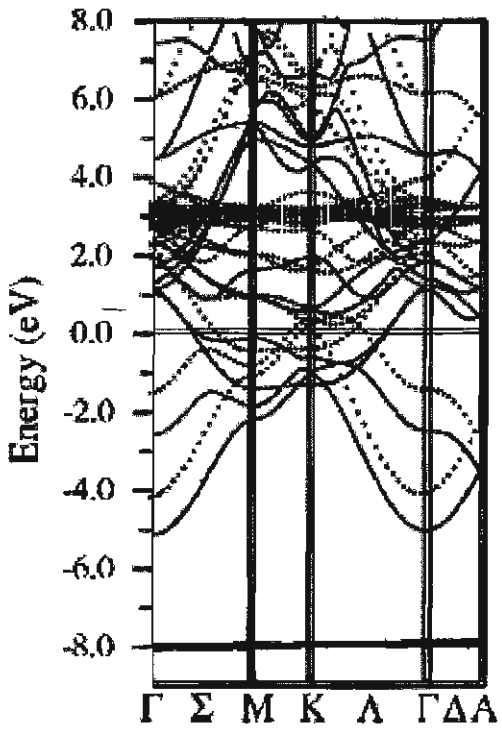

Figure 1.11: Band structure of Gd using LSDA+U for spin-up (solid lines) and spin-down (dotted lines) states. Fermi energy is at 0 eV by Sapan *et al.* [20].

Victor Antonov [23] employed the Local Density Approximation (LDA + U) to calculate the electronic band structure of Gd. Fig 1.14 emphasizes the band structure in the energy range between -1.0 and 1.0 eV which is important to this study in the infrared range. The coloured vertical lines show the possible interband transitions. The thickness of the lines indicates the strength of the transition probability.

There are three essential points to be concluded from the band structure studies of

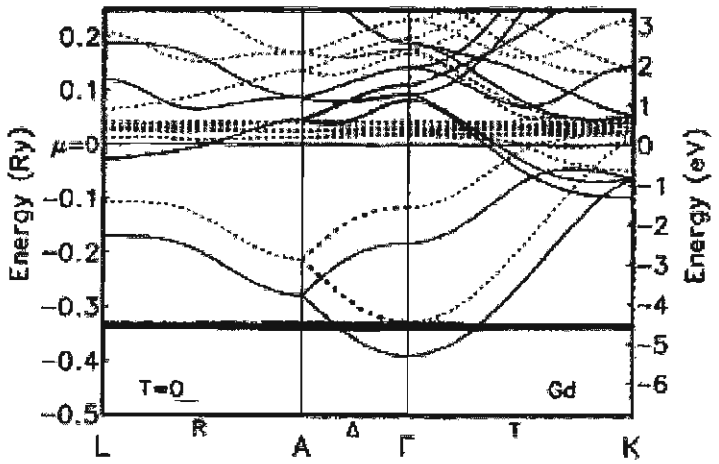

Figure 1.12: Spin-resolved T= 0 bandstructure of Gd ás a function of wave-vector, obtained from ASW calculation. Solid lines for spin-up states, broken lines for spin-down states by Nolting *et al.* The chemical potential μ defines the energy zero [13]. Recall 1 Ry=13.6 eV.

Gd. (i) Between different authors the agreement is satisfactory about the dispersion of the conduction bands at the Γ point. Harmon and Demmock pointed out the fact that the conduction bands are rather insensitive to changes in the potential used as an input to the different calculation methods [21] [17]. (ii) There is a disagreement between some of the studies about the position of the $4f$ bands and the splitting energy of these bands. This disagreement can be attributed to the strong sensitivity of these quantities for $4f$ on the potential used as suggested by Demmock [17]. However, most of the studies agree about the narrow width of the $4f$ bands indicating that these band are highly localized. (iii) The exchange splitting of the conduction bands is temperature dependent and anisotropic in the k-space [22], [24], [21], [20].

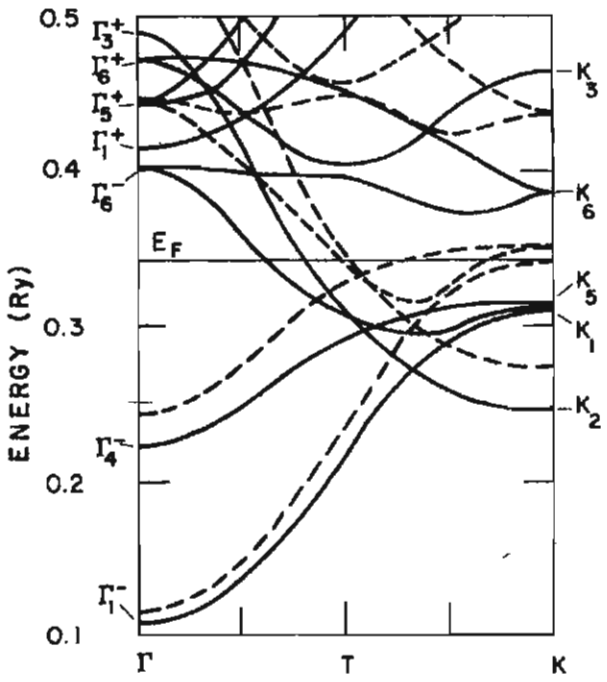

Figure 1.13: Spin-up (solid curves) and spin-down (dashed curves) energy bands in ferromagnetic Gd metal plotted along Γ to K from calculations by Harmon and Freeman [21]. Recall 1 Ry=13.6 eV.

1.1.4 Optical Properties of Gadolinium

Reviewing the previous work on Gd reveals a substantial disagreement between different researchers. This section will present some of the experimental data available for the optical properties of Gd and compare them.

Optical Reflectivity

The effect of the magnetic ordering on the optical properties of the rare earth metals is of great interest for many theoretical and experimental researchers. Miwa [25] suggested the possibility of observing an optical absorption as a result of the magnetic

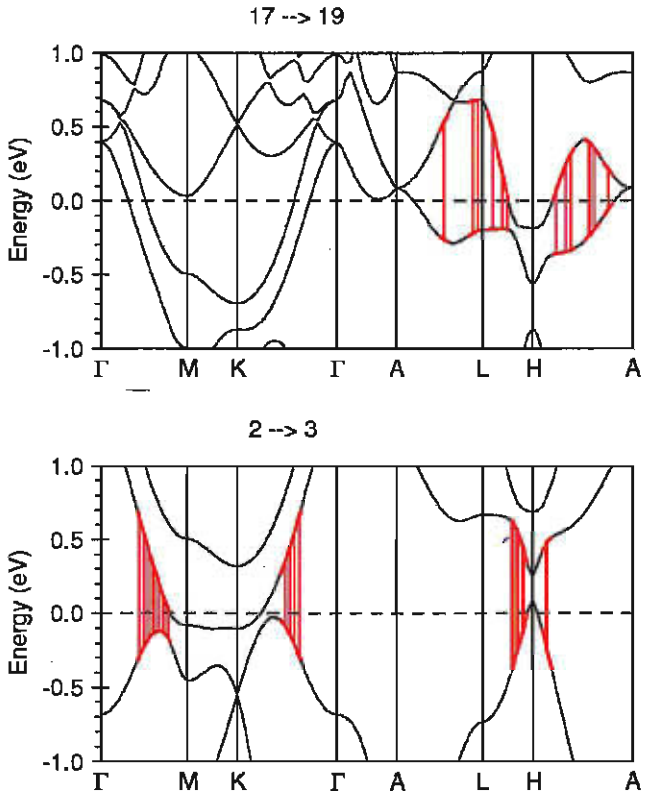

Figure 1.14: Band structure of Gd calculated by Antonov [23]. The vertical lines show parts of k-space where stronger optical transitions occur.

ordering in these metals. Schuler[26] showed that there is a considerable difference in the reflectivity in the paramagnetic and ferromagnetic states of Gd as shown in Fig. 1.15.

Weaver and Lynch [27] studied a Gd single crystal at near-normal incidence using a polarized radiation at 4.2 K between 0.2 and 4.4 eV. The lowest energy for which there is optical data is 0.2 eV. The crystal was cut to expose the c-axis to the incident beam. The sample was mechanically polished and then electropolished to remove any

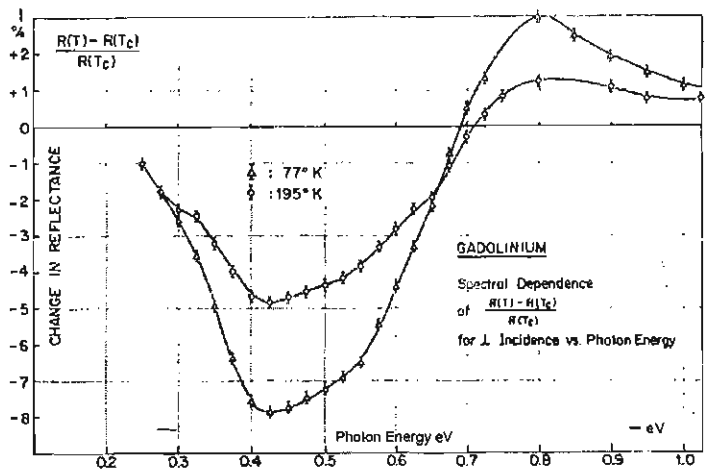

Figure 1.15: Change in the reflectivity versus photon energy upon magnetic ordering for Gd thin film at 77 K and 195 K by Schuler[26]. Recall 1 eV$\simeq$ 8064 cm^{-1}.

possible damage. Changing the polarizer enabled them to study both orientations with the same sample. The measured absorptivity A (A=1 - R where R is the reflectivity), is shown in Fig. 1.16. Converting this data to reflectivity has shown a broad peak in the reflectivity centered at about 2.5 eV Fig. 1.17.

Fig. 1.18 presents the reflectivity of an evaporated polycrystalline film at room temperature from Blodgett [28]. The lower portion of Blodgett's reflectivity data between 1-3 eV decreases linearly. Also, the high frequency reflectivity shows a sharp structure at about 3.7 eV and a broad structure near 8 eV. Note the absence of the broad peak that was seen in Weaver's data about 2.5 eV in Fig. 1.17. Note also, the difference in the absolute value of the reflectance from both authors, For example Blodgett's reflectance is about 10% higher than Weaver's reflectance at 1 eV.

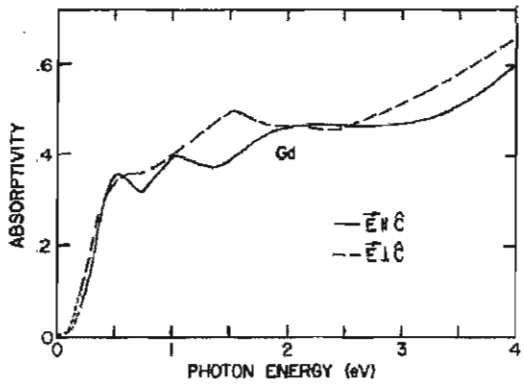

Figure 1.16: Optical absorptivity of Gd single crystal at 4.2 K by Weaver and Lynch [27].

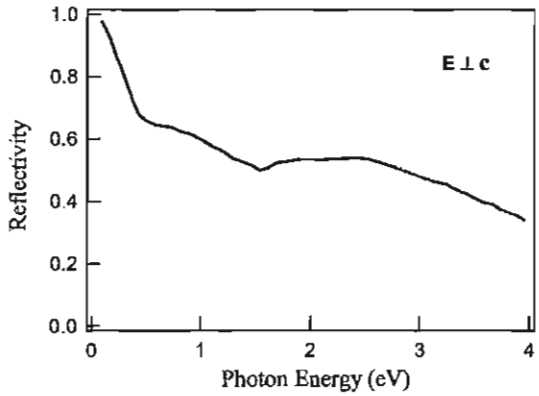

Figure 1.17: Optical reflectivity of Gd single crystal at 4.2 K from Weaver and Lynch [27].

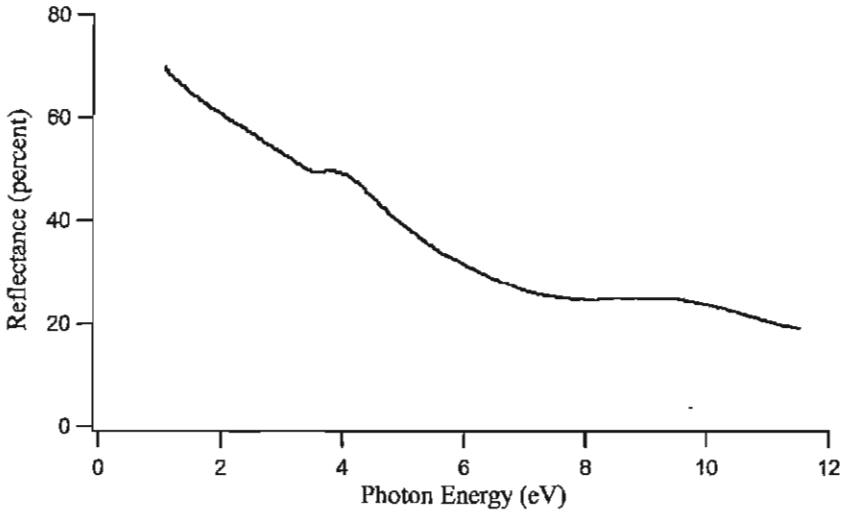

Figure 1.18: Optical reflectivity of Gd evaporated polycrystalline film by Blodgett [28].

Optical conductivity

The optical conductivity is the electrical conductivity in presence of an alternating electric field. The study of the electric conductivity, which is related to the dielectric

function , provides some information about the band structure and the possible electronic transitions. Often the experimental data of the reflectance or transmittance is used to determine the optical conductivity as a function of frequency. Also, the optical conductivity can be calculated theoretically from the band structure. Sapan *et al.* [20] have calculated the diagonal as well as off-diagonal components of the interband optical conductivity tensor. Fig. 1.19 shows the resulting optical conductivity. It should be taken into account that Sapan did not include the intraband transitions in his calculations. Therefore his results in the low energy is not presise because the intraband transitions are dominant at low energy. Table 1.1 gives the conversion factors for the different units used for the optical conductivity.

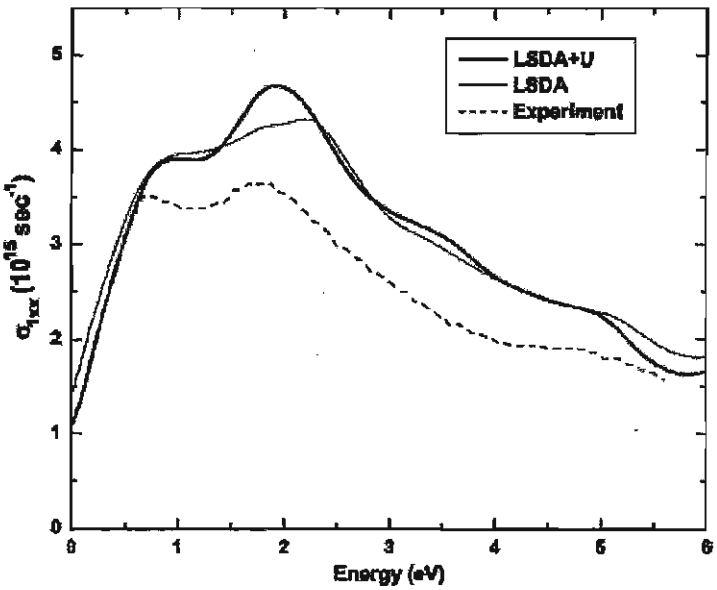

Figure 1.19: The real part of the optical conductivity calculated by Sapan *et al.* The experimental data are from Erskine and Stern [29]. Note that by calculation $\sigma(2eV) \approx 5000\ \Omega^{-1}\ \mathrm{cm}^{-1}$ [20].

The optical conductivity determined by Kramers - Kronig analysis form experimental data of Weaver is shown in fig (1.20). They observed a structure at the

Ω^{-1} cm^{-1}	Statohm-cm (esu)	s^{-1}
1	8.984 $\times 10^{11}$	8.984 $\times 10^{11}$

Table 1.1: Units conversion of the optical conductivity

energies 0.52 eV, 1.05 eV, and near 2.5 eV considering both orientations.

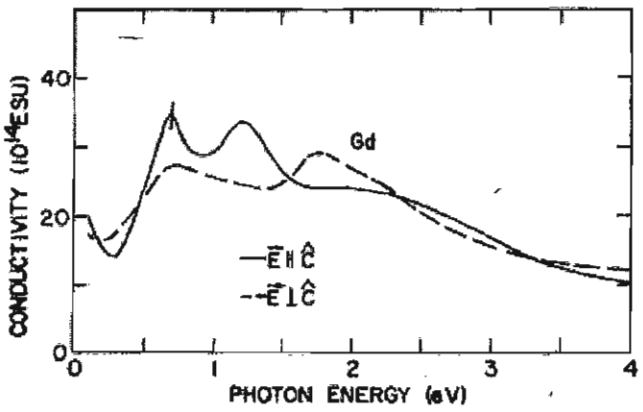

Figure 1.20: Optical conductivity of Gd a single crystal at 4 K [27]. Note that the peak for E=0.7 eV $\approx$ 2500 Ω^{-1} cm^{-1}.

Knayazev *et al.* [30] studied Gd single crystal in the energy range between 0.3 and 5 eV using a polarimetric method in the temperature range 80 - 293 K for both polarization of the incident beam, E $\parallel$ c and E $\perp$ c. The resulting dispersion optical conductivity is shown in Fig. 1.21. They have observed an anomaly at 0.7 eV which appears only below T_c. Notice that this value is lower than the position of the peak reported by Weaver by about 0.18 eV. But they were not able to observe the broad peak about 2.5 eV in the ferromagnetic state. Instead their conductivity data for E $\perp$ c shows a broad peak centered at 1.7 eV. This peak exists for both 80 K and 293 K.

The experimental studies of the optical properties of Gd has been done mostly

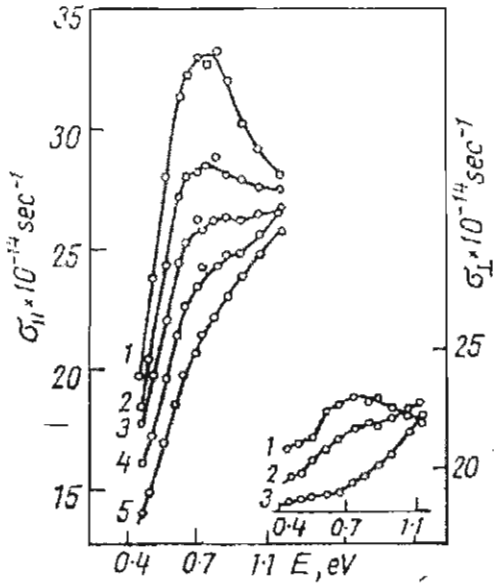

Figure 1.21: Optical conductivity of single crystal gadolinium at different temperatures $\sigma_{\parallel}$ 1- 80K, 2- 160K, 3- 200K, 4- 240K, 5- 293K. $\sigma_{\perp}$ 1- 80K, 2- 160K, 3- 293K by Knayazev *et al.* [30]. Note that the peak in $\sigma_{\perp}$ at E=0.7 eV $\approx 2500\ \Omega^{-1}\ cm^{-1}$ for T=80 K.

on film samples because of the material's high reactivity. The deposition of a thin film in high vacuum to the base of a silica prism assures the purity and absence of oxidation [6]. In the studies of the film samples, Petrakian *et al.* [31] studied a thick deposit (purity 99.99 %) in the energy range 0.5 -1.5 eV in order to examine the s-f exchange energy. They observed a pronounced peak near 0.69 eV due to the expected magnetic affect. Fig (1.22) shows the optical conductivity of Patrikian's work along with Hodgson's data for film samples [32] and Knyazev's data for a polycrystalline sample [33]. From Fig. 1.22 it is obvious that there is a huge discrepancy between the data from different authors.

Krizek *et al.* [34] showed that the pronounced peak in the optical conductivity Fig. 1.23 around 0.7 eV gradually decreases as the temperature increases towards T_c

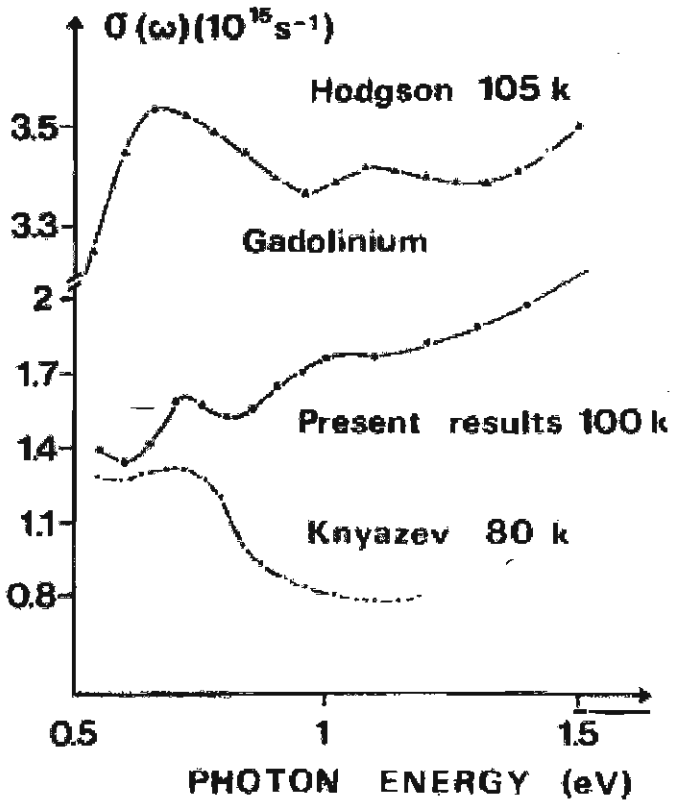

Figure 1.22: Optical conductivity of Gd from Petrakian [31] compared to the results of Hodgson [32] and Knayazev [33]. Recall 9×10^{11} $s^{-1} = 1$ Ω^{-1} cm^{-1}.

and eventually develops into a minimum at 293K. In his work Krizek was not able to observe the 1.1 eV peak reported by Hodgson [32] and others. Also, they investigated the discrepancy between the different thin film data available from other researchers by making measurement on oxidized film. He concluded that the disagreement is most likely due to the effect of the substrate. Explaining that the mismatch between the substrate and the deposited metal produces an interface layer of disordered crystal structure giving a minimum thickness of 400 Å of the thin film to show this effect and deviate from the bulk material properties.

Table 1.2 summarize the different values of the peak in the optical conductivity

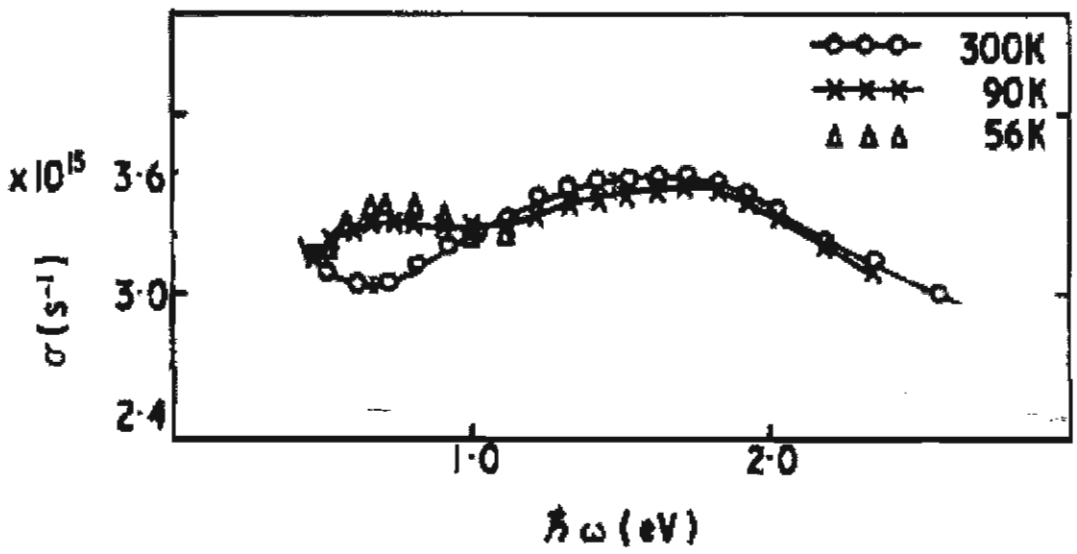

Figure 1.23: Optical conductivity of Gd film at 300, 90 and 56 K versus the photon energy by Krizek *et al.* [34].

about 0.7 eV from different authors and different kinds of samples. It is clear from the table that there is a good agreement in the low frequency observations for both the position of this peak and the value of the optical conductivity. The type of the sample and the temperature variation of these studies should be taken into account. On the other hand, reviewing the high frequency peaks in the optical conductivity through these studies show a huge disagreement. For instance the peaks at about 1.0 eV and 2.0 eV exist in some studies while not in other studies.

Quemerais *et al.* [35] attempted to clarify the disagreement too. They evaluated the reflectance of Gd thin film at different times during the oxidation process. They showed an almost identical reflectance shape. But, the magnitude of the reflectance lowered significantly with time. Also they noticed that the dip in the reflectance around 7.0 eV is shifting towards lower energy with oxidation, and noted that the absorption threshold of Gd oxide is 5.5 eV.

Author	Sample type	T (K)	σ (Ω^{-1} cm^{-1})	position (eV)
Antonove [23]	Calculation	0	3000	0.6
Sapan [20]	Calculation	0	3500	0.65
Erskine and Stern [29]	Thin film	105	3150	0.65
Weaver [27]	Single crystal	4.2	2500	0.7
Knayazev *et al* [30]	Single crystal	80	2500	0.7
Petrakian [31]	Thick film	100	1395	0.7
Hodgson [32]	Thin film	105	3150	0.7
Krizek [34]	Thin film	90	3000	0.7
Knayazev [33]	Polycrystalline	80	1170	0.7

Table 1.2: Summary of the absolute values of the peak in optical conductivity around 0.7 eV from different authors.

Quemerais [35] was able to separate the interband contributions to the optical conductivity from the intraband contributions by subtracting the free electron part (calculated from Drude model of optical conductivity) from the experimental data. This method will become clear in chapter 2. Fig. 1.24 shows that the intraband contribution dominates at low energies.

This thesis consists of four chapters. The next three chapters will be as follows: Chapter 2 will discuss the theory of the optical constants of solids. This chapter explains the methods of modeling the dielectric function, as well as the Kramers Kronig method of analysing the optical data. Chapter 3 describes in details the preparation of the sample for the optical measurement. It will explain the experimental method used in this work as well. Chapter 4 will present the experimental data and the resulting optical functions and discuss them. This chapter also attempts to explain the

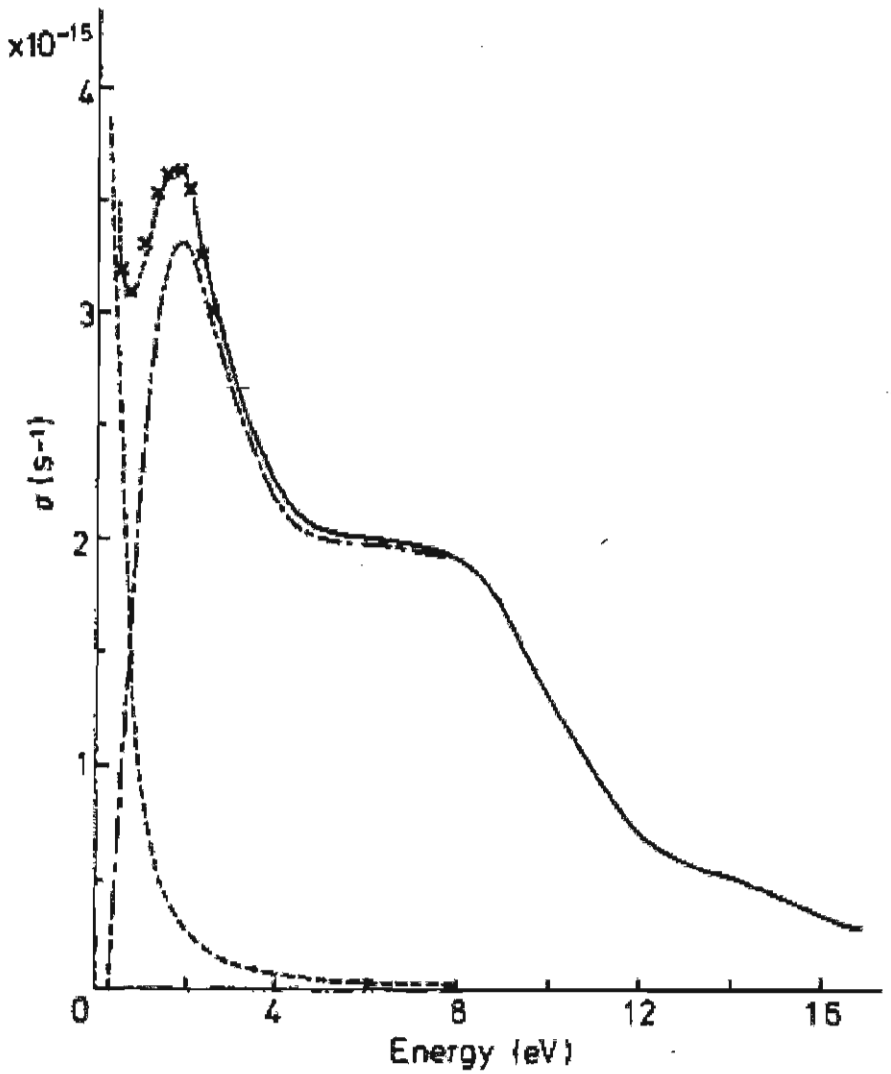

Figure 1.24: Experimental determination of the real optical conductivity at 300 K by Quemerais *et al.* [35] — , the results of Hodgson *et al.* [32] × - - × - -, intraband part according to σ_0 and τ (given in the text) from Hodgson *et al* [32]- - - -, and interband part (experimental minus intraband part) — - — . Recall 9×10^{11} $s^{-1} = 1$ Ω^{-1} cm^{-1}.

behaviour of the optical function particularly in the low frequency region and tries to compare them with the available theoretical and experimental data.

Chapter 2

Optical properties of solids

Studying the optical properties of solids provides information about the electronic structure of materials. Because the optical response functions are related to the electronic excitation at the atomic level [18],[36],[37], these constants will have certain features at particular frequencies. These functions are significantly altered by changes in the chemical composition, temperature variation or magnetic ordering [18]. Therefore studying them is a source of more information about materials. This chapter discusses the optical response functions and how to extract them from optical reflectivity data.

2.1 Reflectivity

One of the most powerful methods to probe the optical properties of solids and hence their microscopic properties is measuring the reflectivity which is the ratio of the reflected power to the incident power on the surface denoted by the symbol R [37].

The electromagnetic waves can interact with the material by inducing a transition between vibrational states, between electronic states inside the conduction band (intraband transitions) or between electronic states in different bands (interband transitions). If the incident light has a sufficient amount of energy it will be absorbed by the electrons in the occupied states below the Fermi level to unoccupied states above the Fermi level [36]. Measuring the optical reflectivity is one of the most powerful

ways to determine these energies.

The interaction of electromagnetic waves with the material can be described by Maxwell's equations :

$$\nabla \cdot \mathbf{E} = \frac{\rho^{total}}{\epsilon_0} \tag{2.1}$$

$$\nabla \times \mathbf{E} = -\frac{\partial \mathbf{B}}{\partial t} \tag{2.2}$$

$$\nabla \cdot \mathbf{B} = 0 \tag{2.3}$$

$$\nabla \times \mathbf{B} = \mu_0 \epsilon_0 \frac{\partial \mathbf{E}}{\partial t} + \mu_0 \mathbf{J}^{total} \tag{2.4}$$

$\mathbf{E}$ and $\mathbf{B}$ are the electric and magnetic fields, respectively. ρ^{total} and $\mathbf{J}^{total}$ are the total charge and current densities, respectively. ϵ_0 and μ_0 are the permittivity and permeability of free space , respectively. One of the solutions of these equations in the free space (ρ^{total}=0 and $\mathbf{J}^{total}$=0) is the plane wave solution which is given by:

$$\mathbf{E} = \mathbf{E}_0 exp^{i(\mathbf{k}.\mathbf{r}-\omega t)} \tag{2.5}$$

$$\mathbf{B} = \mathbf{B}_0 exp^{i(\mathbf{k}.\mathbf{r}-\omega t)} \tag{2.6}$$

Where $\mathbf{k}$ is the wave vector, t is the time, and $\mathbf{r}$ is the spatial vector. Applying this solution to Eq. 2.2 yelds:

$$|\mathbf{B}| = \frac{1}{c} |\mathbf{E}| \tag{2.7}$$

Where c is the speed of light. If an electromagnetic wave incident on a medium, as shown in Fig. 2.1, replacing ϵ_0 by ϵ, μ_0 by μ then $\mathbf{B}$ will be given by: $|\mathbf{B}| = \frac{n}{c} |\mathbf{E}|$ where n is the index of refraction. Applying the appropriate boundary conditions on the incident, reflected and transmitted beams at the interface between vacum $n_1 = 1$ and a non-magnetic medium with index of refraction n as follows:

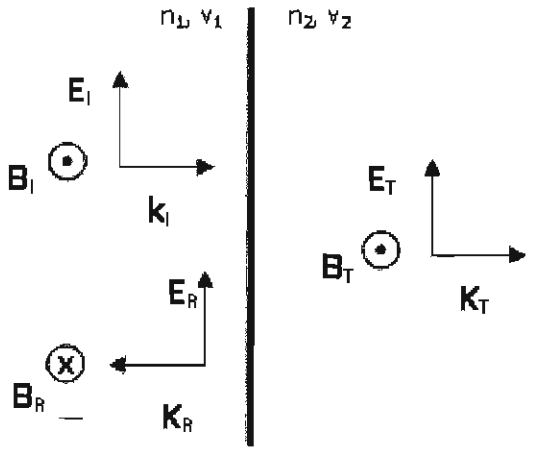

Figure 2.1: Schematic plot of normal incidence of an electromagnetic wave on the interface between two media.

$$E_i + E_r = E_t \tag{2.8}$$

$$\frac{B_i}{\mu_o} - \frac{B_r}{\mu_o} = \frac{1}{\mu_2} B_t \tag{2.9}$$

Where μ_o and μ_2 is the magnetic permability in air and the medium, respectively. By substituting $B_i = \frac{E_i}{c}$, $B_r = \frac{E_r}{c}$ in the last two equations and solving them for E_i results into one Fresnel equation:

$$\frac{E_r}{E_i} = \frac{\sqrt{\mu} - \sqrt{\tilde{\epsilon}}}{\sqrt{\mu} + \sqrt{\tilde{\epsilon}}} = \frac{1 - \sqrt{\frac{\tilde{\epsilon}}{\mu}}}{1 + \sqrt{\frac{\tilde{\epsilon}}{\mu}}} \tag{2.10}$$

Where E_i and E_r are the incident and reflected electric field strengths, respectively. Since the intensity of light is proportional to $\mathbf{E}\mathbf{E}^*$ Eq. 2.10 can be rewritten as[37] :

$$R = \frac{I_r}{I_i} = \left| \frac{E_r}{E_i} \right|^2 = \left| \frac{1 - \sqrt{\frac{\tilde{\epsilon}}{\mu}}}{1 + \sqrt{\frac{\tilde{\epsilon}}{\mu}}} \right|^2 \tag{2.11}$$

Where I_r and I_i the incident and reflected light intensities. The complex index of refraction $\tilde{n}$ for a magnetic material with magnetic permeability μ can be given in

terms of the complex dielectric function $\tilde{\epsilon}$ as follows [36]:

$$\tilde{n} = \sqrt{\tilde{\epsilon}\mu} \tag{2.12}$$

2.2 Optical response functions

The optical properties of a material can be determined by the complex dielectric function $\tilde{\epsilon}$ or the complex index of refraction $\tilde{n}$ which are given by:

$$\tilde{\epsilon} = \epsilon_1 + i\epsilon_2 \tag{2.13}$$

$$\tilde{n} = n + ik \tag{2.14}$$

The imaginary part of the complex index of refraction k is called the extinction coeffecient and it is related to the absorption process inside the medium [37].

The complex optical conductivity $\tilde{\sigma}$ represents the response of the material to the applied transverse electric field [36] and it is given by:

$$\tilde{\sigma} = \sigma_1 + i\sigma_2 \tag{2.15}$$

The real and imaginary parts of the optical conductivity are related to the complex dielectric function as:

$$\sigma_1 = \omega\epsilon_0\epsilon_2 \tag{2.16}$$

$$\sigma_2 = -\omega\epsilon_0\epsilon_1 \tag{2.17}$$

It is useful to write n and k in terms of the complex dielectric function[37]. And considering a magnetic material (recall equation 2.12) We have:

$$n = \frac{\sqrt{\mu}}{\sqrt{2}}\sqrt{\epsilon_1 + \sqrt{{\epsilon_1}^2 + {\epsilon_2}^2}} \tag{2.18}$$

$$k = \frac{\sqrt{\mu}}{\sqrt{2}}\sqrt{-\epsilon_1 + \sqrt{{\epsilon_1}^2 + {\epsilon_2}^2}} \tag{2.19}$$

2.3 Modeling the complex dielectric function

2.3.1 Drude Lorentz model

The Drude Lorentz model is based on the assumption that the electrons are bound to the atom by a spring [37]. The electric field of the incident beam of light will cause a driving force -eE that acts on the electrons. The electron will oscillate as a damped harmonic oscillator with Hook's restoring force $-k\vec{r}$, and a frictional damping force which is proportional to the velocity of the electron $m\Gamma\frac{d\vec{r}}{dt}$, with m the electron mass, e the electron charge and k the spring constant which can be rewritten as $m{\omega_o}^2$, where ω_o is the resonance frequency of the oscillator. The equation of motion of these electrons is given by:

$$m\frac{d^2r}{d^2t} + m\Gamma\frac{dr}{dt} + m\omega_o r = -eE \tag{2.20}$$

substituting the real part of the electric field and from Eq. 2.5 and the real part of $r = r_0 exp^{i(\mathbf{k}.\mathbf{r}-\omega t)}$ we can find the displacement of the electron from the equilibrium position :

$$r_0 = \frac{\frac{-eE_0}{m}}{{\omega_o}^2 - \omega^2 - i\Gamma\omega} \tag{2.21}$$

This gives the resonant polarization [37]

$$P_{resonant} = \frac{Ne^2}{m}\frac{1}{{\omega_o}^2 - \omega^2 - i\Gamma\omega}E \tag{2.22}$$

Since the electric displacement is related to the electric field and the polarization for an isotropic material can be rewritten as:

$$\mathbf{D} = \epsilon_o\epsilon_r E \tag{2.23}$$

combining equations 2.22 and 2.23 gives the complex dielectric function in terms of the scattering rate Γ and the resonant frequency $\omega_\circ$ and the plasma frequency ω_p as follows:

$$\epsilon_1(\omega) = 1 + \frac{{\omega_p}^2({\omega_\circ}^2 - \omega^2)}{({\omega_\circ}^2 - \omega^2)^2 + \Gamma^2\omega^2} \tag{2.24}$$

$$\epsilon_2(\omega) = \frac{{\omega_p}^2\Gamma\omega}{({\omega_\circ}^2 - \omega^2)^2 + \Gamma^2\omega^2} \tag{2.25}$$

where ${\omega_p}^2 = \frac{Ne^2}{m}$ and N is the number of electrons per unit volume.

2.3.2 Drude model

The Drude model for the dielectric function is used to model the free electron response in a metal. Since in a metal the electrons are free the restoring force is zero. Which means that $\omega_\circ$ can be set to zero. It is obvious from equations 2.24 and 2.25 that these quantities for matal can be written as :

$$\epsilon_1(\omega) = 1 - \frac{{\omega_p}^2}{\omega^2 + \Gamma^2} \tag{2.26}$$

$$\epsilon_2(\omega) = \frac{{\omega_p}^2\Gamma}{\omega(\omega^2 + \Gamma^2)} \tag{2.27}$$

From Eq. 2.16 the real part of the optical conductivity is given by:

$$\sigma_1 = \frac{\epsilon_0{\omega_p}^2\Gamma}{\omega^2 + \Gamma^2} \tag{2.28}$$

The zero frequency limit of the optical conductivity is the *dc* conductivity :

$$\sigma_{dc} = \frac{1}{\rho_{dc}} = \frac{\epsilon_0{\omega_p}^2}{\Gamma} \tag{2.29}$$

In general, to fit experimental data the dielectric function is modeled by one Drude term and a number of oscillators corresponding to either phonon or electronic absorp-

tion:

$$\epsilon(\omega) = \epsilon_\infty - \frac{{\omega_p}^2}{\omega(\omega + i\Gamma)} + \sum_j \frac{{\omega_{p,j}}^2}{({\omega_{o,j}}^2 - \omega^2) - i\omega\Gamma_j} \tag{2.30}$$

where ϵ_∞ is the constant contribution of high frequency oscillators in the experimentally measured range.

2.3.3 Approximations for metals

The frequency dependence of the reflectivity R for a typical metal (free electron metal) is shown in Fig.2.2. This curve is calculated according to the Drude model. In the

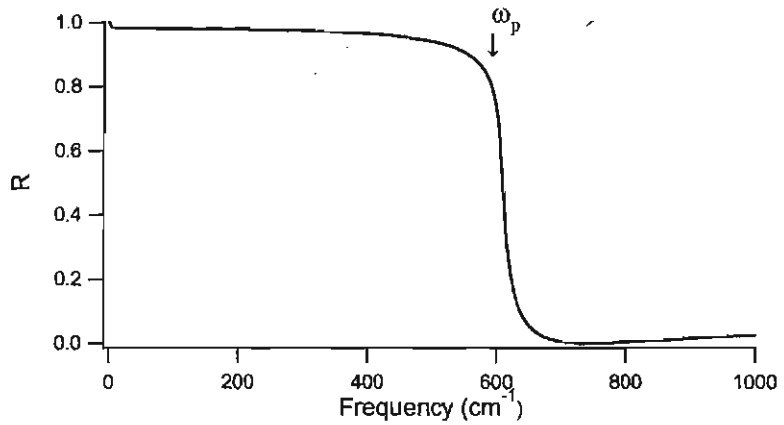

Figure 2.2: Reflectivity of Drude metal

region of very low frequency where $\omega \ll \Gamma$ the normal reflectance is given by:

$$R(\omega) \simeq 1 - \frac{2^{\frac{3}{2}}\Gamma^{\frac{1}{2}}}{\omega_p}\omega^{\frac{1}{2}} \tag{2.31}$$

This formula is the Hagen-Ruben approximation.

In the frequency region where $\Gamma \ll \omega \ll \omega_p$ the reflectance of a typical metal is frequency independent and is given by:

$$R(\omega) \simeq 1 - \frac{2\Gamma}{\omega_p} \tag{2.32}$$

A metal could show a deviation from the Drude model when a temperature dependence is detected in this region. At high frequencies where the approximations $\epsilon_1 \simeq 1$ and $\epsilon_2 \simeq 0$ are valid, the reflectivity is given by

$$R(\omega) \simeq \frac{1}{16}\frac{{\omega_p}^4}{\omega^4} \tag{2.33}$$

2.3.4 Reflection from multilayer systems

In case there was a Gd_2O_3 layer on a Gd sample, one has to treat the whole sample as a multilayer system of two layers. Fig. 2.3 presents a multilayer system of N layers. Each layer is assumed to be isotropic and has a certain dielectric function ϵ , an index of refraction n, and a thickness d. To derive an expression for the reflectance and transmittance through the whole system, the appropriate boundary conditions should be applied at each interface. Therefore, it is possible to write the wave amplitude at each layer in terms of the incident wave[38].

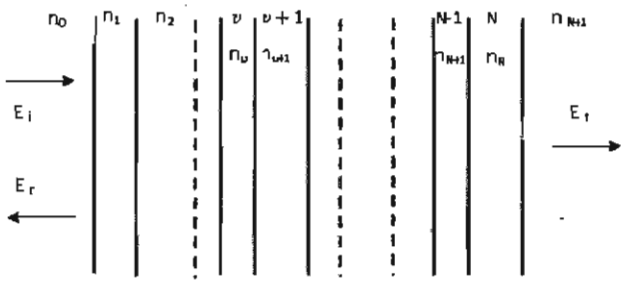

Figure 2.3: Multilyer system

In case of normal incidence, the resulting reflectance and transmittance can be written in terms of a set of 2 × 2 matrices. The matrix is a function of the Fresnel coefficients and given by:

$$M_\nu = \begin{pmatrix} exp^{i\delta_{\nu-1}} & r_\nu exp^{i\delta_{\nu-1}} \\ r_\nu exp^{-i\delta_{\nu-1}} & exp^{-i\delta_{\nu-1}} \end{pmatrix} \tag{2.34}$$

where $\delta_\nu = 2\pi\omega n_\nu d_\nu$ is the phase thickness of the nth layer. r_ν is the Fresnel reflection coefficient at $\nu/\nu - 1$ boundary.

For the normal incidece from the $n_\circ$ side :

$$R = \frac{m_{21}}{m_{11}} \tag{2.35}$$

$$T = \frac{\prod_{\nu=1}^{N+1} t_\nu}{m_{11}} \tag{2.36}$$

Where m_{11} and m_{21} are the elements of the product matrix :

$$\prod_{\nu=1}^{N+1} M_\nu = \begin{pmatrix} m_{11} & m_{12} \\ m_{21} & m_{22} \end{pmatrix} \tag{2.37}$$

Therefore, the reflection and transmittance are given by :

$$\mathbf{R} = RR^* \tag{2.38}$$

$$\mathbf{T} = \frac{n_{N+1}}{n_\circ} TT^* \tag{2.39}$$

Alexy Kuzmenko [39] has written a program to fit the normal incidence reflection of a sample consisting of an arbitrary number of layers [40]: His model is based on the physics discussed above. To use the RefFit software by Kuzmenko, the input needed to simulate the reflection of a whole system is the thickness and the complex dielectric function of each layer.

2.3.5 Kramers- Kronig relations

The linear response of the medium [36] [18] to a stimulus acting at time t' can be given in general by :

$$\chi(t) = \int_{-\infty}^{\infty} G(t - t') f(t') dt' \tag{2.40}$$

where $\chi(t)$ is the response, $G(t-t')$ is the response function, and $f(t')$ is the stimulus. The response function $G(t-t')$ is a function of time and satisfies the causality principle which implies that there is no effect before a cause. Mathematically this can be written as $G(t-t') = 0$ for $t'<t$ since$(t-t')$ is the time interval where the stimulus acts. The Fourier transform of the response function is :

$$G(t-t') = \frac{1}{2\pi}\int_{-\infty}^{\infty} G(\omega)e^{-i\omega(t-t')}d\omega \tag{2.41}$$

Applying the Cauchy integral on $G(\omega)$ gives:

$$G(\omega) = \frac{i}{\pi}\int_{-\infty}^{\infty}\frac{G(\omega')}{\omega'-\omega}d\omega \tag{2.42}$$

$G(\omega)$ in Eq. 2.42 is a complex quantity. The real and imaginary components of this function are:

$$G_1(\omega) = \frac{1}{\pi}P\int_{-\infty}^{\infty}\frac{G_2(\omega')}{\omega'-\omega}d\omega' \tag{2.43}$$

$$G_2(\omega) = \frac{-1}{\pi}P\int_{-\infty}^{\infty}\frac{G_1(\omega')}{\omega'-\omega}d\omega' \tag{2.44}$$

where P stands for the principal value of the integration. Eq. 2.43 and Eq. 2.44 are called the Kramers Kronig relations or K-K relations. The response function can be the optical conductivity $\sigma(\omega)$, the dielectric function $\epsilon(\omega)$ or the complex index of refraction $n(\omega)$. The reflectance in normal incident as given in Eq. 2.10 can be written as :

$$R = \frac{E_r}{E_i} = rr^* \tag{2.45}$$

Where r is the complex reflectivity amplitude which in its polar form is :

$$r(\omega) = \sqrt{R(\omega)}e^{i\theta(\omega)} \tag{2.46}$$

$R(\omega)$ is the real reflectivity which can be measured. $\theta(\omega)$ is the complex phase.

$$ln(r(\omega)) = ln(R(\omega)) + i\theta(\omega) \tag{2.47}$$

Since the reflectance must obey the causality, the K-K pair for $ln(R(\omega))$ and $\theta(\omega)$ from Eq. 2.43 and Eq. 2.44 is as follows:

$$ln(R(\omega)) = \frac{1}{\pi} P \int_{-\infty}^{\infty} \frac{\theta(\omega')}{\omega' - \omega} d\omega' \tag{2.48}$$

$$\theta(\omega) = \frac{-1}{\pi} P \int_{-\infty}^{\infty} \frac{lnR(\omega)}{\omega' - \omega} d\omega' \tag{2.49}$$

Eq. 2.49 allows restoring of the phase function. From Eq. 2.46 $r(\omega)$ can be determined numerically and the real and imaginary parts of the complex index of refraction can be calculated according to the following equations, respectively.

$$n = \frac{1 - r^2}{r^2 - 2rcos\theta + 1} \tag{2.50}$$

$$k = \frac{2rsin\theta}{r^2 - 2rcos\theta + 1} \tag{2.51}$$

The components of the complex dielectric function can be determined from:

$$\epsilon_1 = n^2 - k^2 \tag{2.52}$$

$$\epsilon_2 = 2nk \tag{2.53}$$

The experimental data usually are taken in a limited range of frequency. To apply Eq. 2.49 $R(\omega)$ is needed to be extended to higher and lower frequencies than the experimental range. Eq. 2.49 can be rewritten as :

$$\theta(\omega) = \frac{-1}{2\pi} \int_0^{\infty} \frac{dln\left|R(\omega')\right|}{d\omega'} ln\left|\frac{\omega' + \omega}{\omega' - \omega}\right| d\omega' \tag{2.54}$$

This formula emphasize that only the values of $R(\omega')$ near ω are dominant in this integral because the factor $ln\left|\frac{\omega'+\omega}{\omega'-\omega}\right|$ is sharply peaked at ω. Therefore the integral

from ω_1 to ω_2 contributes strongly to the value of $\theta(\omega)$ The integral outside this range will supply a slow varying contribution to $\theta(\omega)$, but it can be still a considerable distortion to the resulting optical functions [18]

2.3.6 Sum rules

Looking at one atom with Z electrons the sum rule [36] is :

$$\sum_m f_{mn} = Z \tag{2.55}$$

Where f_{mn} is the oscillator strength for transition between states m and n. The analogous sum rule for a solid is given by

$$\int_0^\infty \omega\epsilon_2(\omega)d\omega = \frac{1}{2}\pi{\omega_p}^2 \tag{2.56}$$

This rule comes originally from the derivation of the rate of energy absorbed per unit volume from an electric field for all frequencies. Therefore this sum rule considers all the absorption processes in the frequency range [0,∞]. A typical spectrum includes contributions to the absorption process from phonons, conduction and valence electrons, etc. It is useful to introduce the partial (finite energy) sum rule in terms of the effective number density of electrons contributing to the optical properties up the frequency ω

$$n_{eff}(\omega) = \frac{m}{2\pi^2 e^2}\int_0^\omega \omega'\epsilon_2(\omega')d\omega' \tag{2.57}$$

or in terms of the plasma frequency

$$\int_0^\omega \omega'\epsilon_2(\omega')d\omega' = \frac{\pi}{2}{\omega_{pi}}^2 \tag{2.58}$$

where ω_{pi} is the plasma frequency associated with the isolated absorption. The sum rule above is applicable particularly in systems with well isolated absorptions [18] for instance, the wide band-gap simiconductors where the free carrier absorption is separated from the band to band transitions with a transparent region.

Chapter 3

Experimental Method

3.1 Preparing samples for optical measurement

3.1.1 Gadolinium(III) oxide preparation

Two Gd_2O_3 samples were prepared from a 99.99+% pure Gd_2O_3 powder from Alfa Aesar (CAS# 12064-62-9). To assure no moisture content the powder was calcined at 500°C for 3 hours. Then it was ground to produce equal-sized grain powder. Using a mechanical compressor the powder was compacted into a 13mm diameter tablet. The tablets were sintered in a furnace at 1000°C or 1200°C for about 24 hours. The sintering process helps to produce a solid sample by causing the powder parts to get close and form metallurgical bonds.

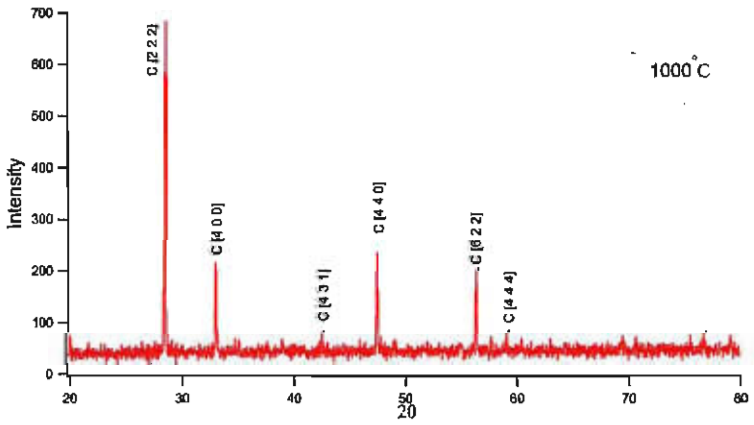

Figure 3.1: XRD spectrum of Gd_2O_3 sintered at 1000°C. C stands for cubic structure.

The crystal structure of these samples was then examined by XRD. Fig.3.2 shows the X- ray diffraction spectrum of the sample sintered at different temperature. The obtained results shows that the sample sintered at 1000°C has cubic structure which is stable at room temperature [41]. While the sample sintered at 1200°C has a mixed phase of cubic and monoclinic structures [41],[42].

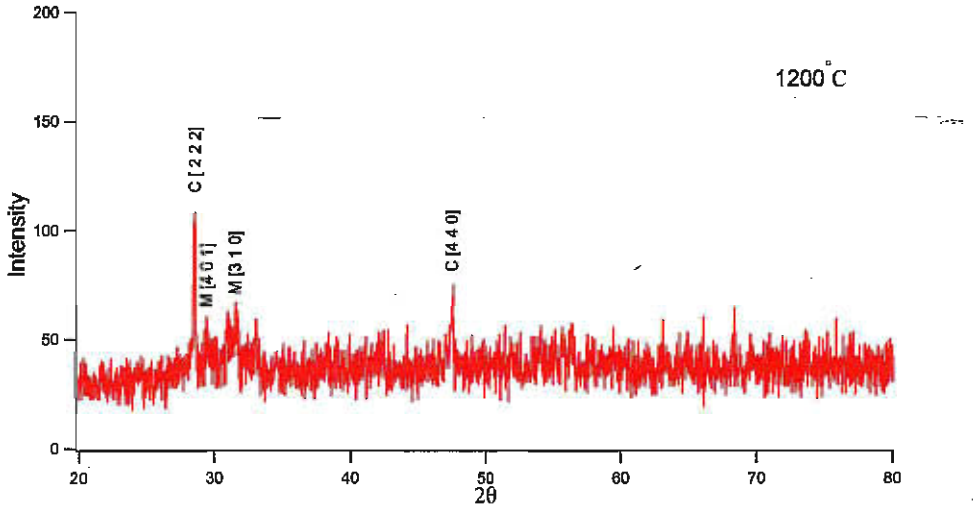

Figure 3.2: XRD spectrum of Gd_2O_3 sintered at 1200°C. C stands for cubic structure and M for monoclinic structure

To obtain a smooth highly reflecting surface for the optical measurement, the two samples were polished down to the smoothness produced by a 1 μm size diamond polishing paste. The cubic Gd_2O_3 sample was used in the measurements.

3.1.2 Gadolinium

A sample of 7 mm x 6 mm x1 mm was cut from a 0001 oriented Gd single crystal produced by Ames National Labs. Before starting this work a Laue diffractogram was taken that shows the (0001) orientation Fig. (3.3). Ames Labs had cut a circular disk out of the sample as shown in Fig. 3.4. It was assumed that the whole sample

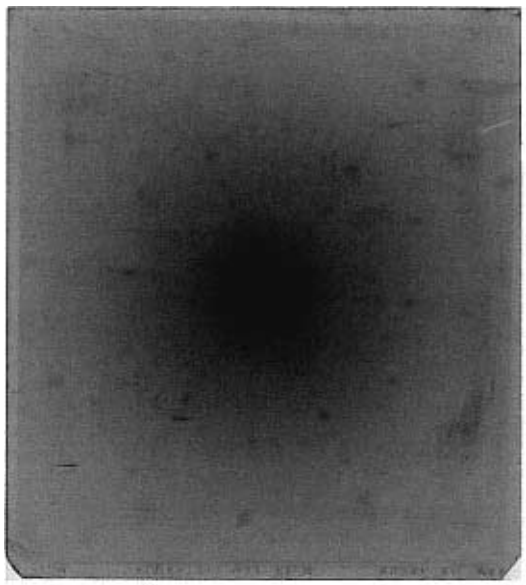

Figure 3.3: The original Laue diffractogram of Gd sample.

was a single crystal which, as will be discussed below, is not correct. A diamond saw was used to cut the sample as shown in Fig. 3.4.

The sample had been exposed to the atmosphere at room temperature for several years. Hence it is expected to be oxidized. Alan *et al.* [44], reported that the oxidation rate of gadolinium can be described by a logarithmic law given by

$$\frac{1}{d} = -0.055log(t) + 0.16 \tag{3.1}$$

t is the time in days and d the thickness in nm.

Equation 3.1 is the best fit of the experimental data of thickness versus time measured at room temperature of Gd thin film. This study showed that the oxidation rate of Gadolinium slows down with time. By calculating the thickness of the oxide layer for 365 days it is about 52.42 nm. Therefore a prt of the sample was polished down to 1 μm grid diamond to remove the oxide layer and establish a reflecting surface. Another piece of the same sample (Fig. 3.4) was left without polishing for the XRD measurement to examine the oxide layer and its properties such as the

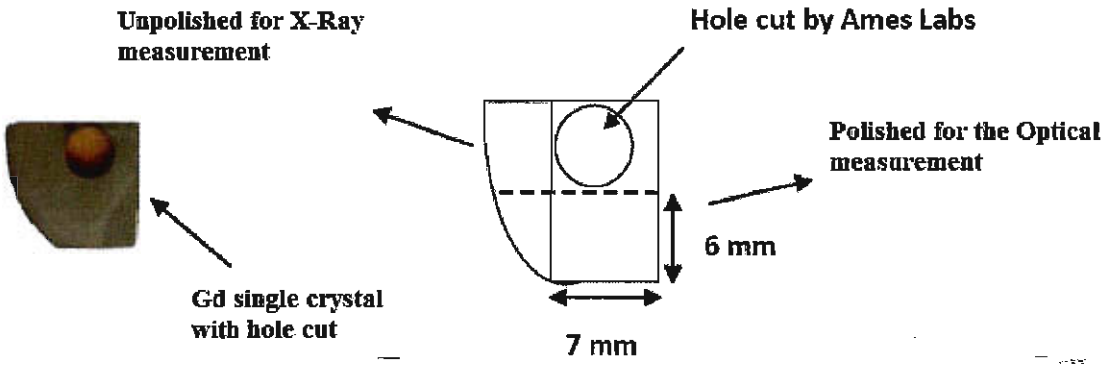

Figure 3.4: Schematic photo out of the sample shows the areas used for XRD and optical measurement.

crystal structure and the thickness. The sample was carefully handled during the optical measurements. It was kept under acetone when not taking measurements to avoid oxidation of the polished face. During the experiments the sample chamber was under high vacuum. Hence, we estimate the exposure time of the Gd sample to air was never more than a couple of hours. Therefore, the thickness of the oxide layer d, if there was any oxidation on the polished sample, is < 6 nm.

The existence of the oxide layer on both samples was examined by XRD. The XRD spectrum of the unpolished Gd sample in Fig. 3.5 shows peaks corresponding to the Gd hexagonal unit cell [43] in addition to peaks from the cubic Gd_2O_3 layer. The estimated thickness of this layer by the X-Ray is on average around 150 ($\pm$50) nm.

Surprisingly, the X-Ray diffraction spectrum of the polished Gd sample in Fig. 3.6

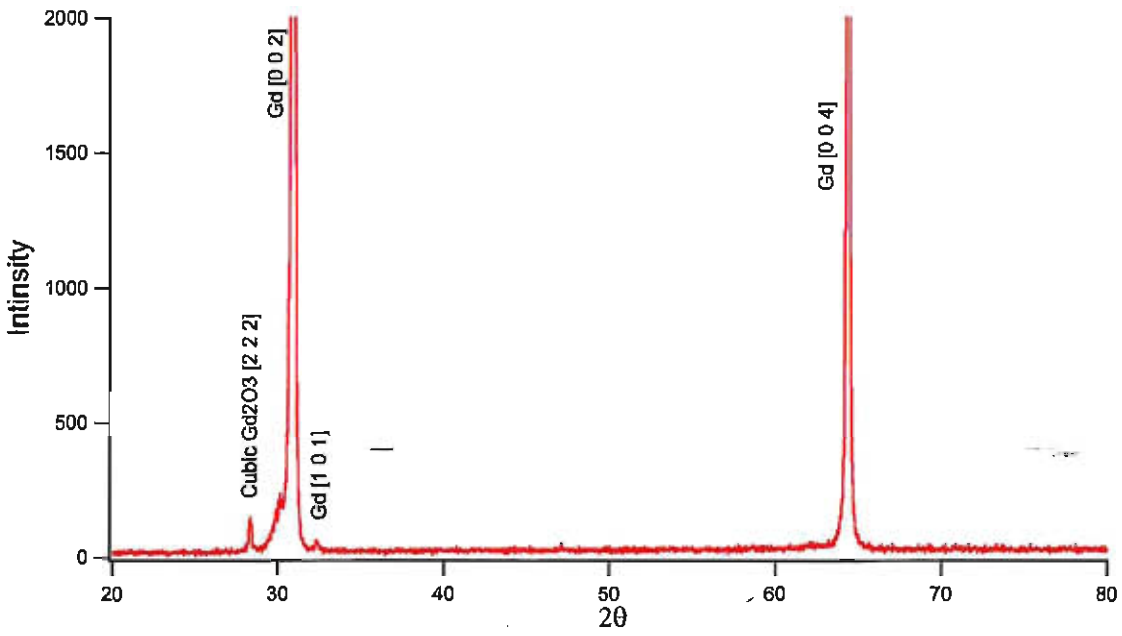

Figure 3.5: XRD spectrum of unpolished Gd sample.

contains low intensity peaks of all the possible diffraction peaks that can be observed for an hcp structure, this indicates that parts of the sample were polycrystalline. Those peaks are believed to be a contribution from the edges of the sample. The cross section of the 2θ scan beam was larger than the crystal, so the diffraction spectrum shown in Fig. 3.6 is an average over all the 7mm x 6mm surface. Therefore there was a need to re-examine the sample using the Laue scattering method with a narrower beam which provides more information about the crystal structure in specific positions on the sample surface.

A Laue scattering measurement was done on different spots on the sample surface. Fig. 3.7 shows a Laue diffractogram of one of the sample corners which appears as a polycrystalline. This may be due to the fact that only parts of the original sample (Fig 3.4) are actually single crystal.

Fig. 3.8 is the Laue diffractogram of the central part of the polished face used for

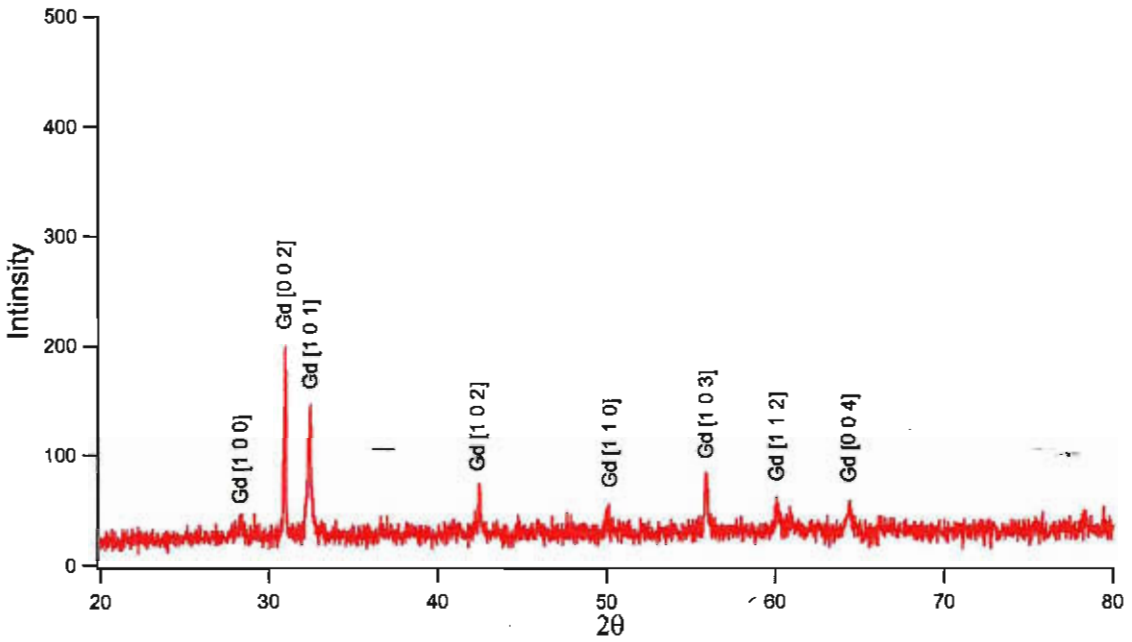

Figure 3.6: XRD spectrum of Polished Gd sample used for optical measurement

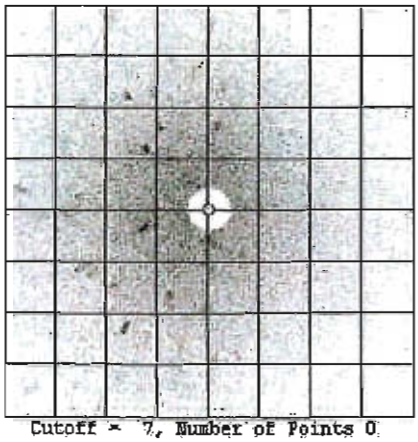

Figure 3.7: Laue diffractogram of the sample corner

the optical measurement and it has the hexagonal symmetry of a Gd single crystal. As will be described in the next section the light beam can be focussed into a small area on the sample using an aperture during measurement. Hence we are confident that our optical measurements are for a (0001) orientation of the Gd surface.

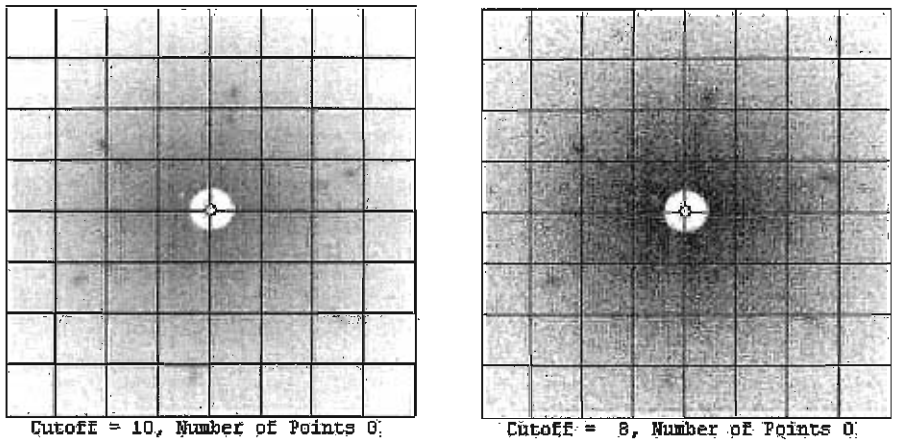

Figure 3.8: Laue diffractogram of two spots in the centre of the polished sample surface.

3.2 Optical measurement

IFS 66V/S Bruker spectrometer was used to measure the optical reflectance of the samples. The IFS 66V/S is a flexible vacuum FT-IR spectrometer whose spectral range may be expanded from far infrared (FIR) to near UV [45].

A set of mirrors have been added to the spectrometer to direct the light beam to an external JANIS [model No:ST 400] sample cryostat through an optical window and then to the detector. More details will be given below.

3.2.1 Interferometer

The interferometer consists of two mirrors and a beamsplitter. One mirror is fixed and the other moving. The configuration of these component is the same as a Michelson interferometer which is shown in Fig. 3.9. But in the Bruker spectrometer the interferometer is controlled by a computer using the OPUS/IR software which allows setting the velocity of the moving mirror. In addition, some manipulation can be done on the resulting spectra such as dividing or subtracting processes.

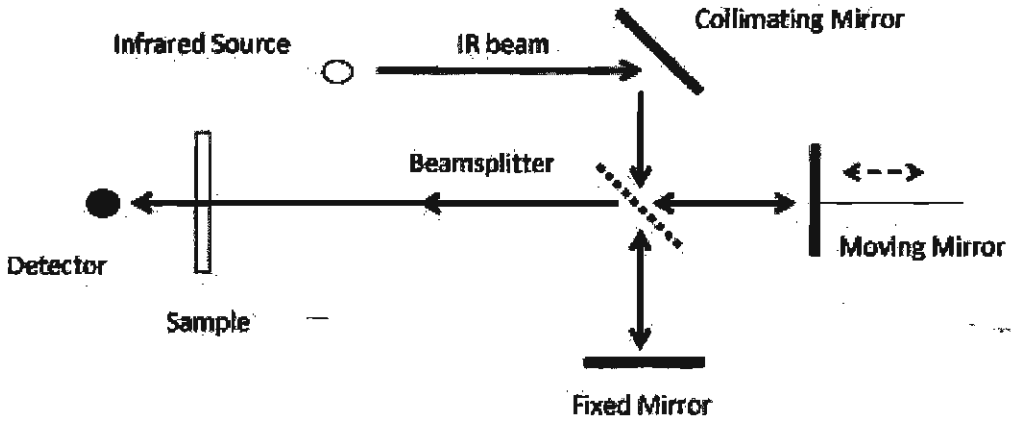

Figure 3.9: Michelson interferometer

As illustrated in Fig. 3.9 the source emits a broad band beam of light which strikes the beam splitter. The beam splitter splits the incoming beam into two beams with roughly equal intensities by transmitting half and reflecting the other half. The transmitted beam reflects off the fixed mirror. While the reflected beam strikes the moving mirror. The returning beams combine at the beam splitter. The motion of the moving mirror will cause a path difference between the two beams which results in a constructive interference when the path difference is an integer number of the wavelength, and a destructive interference if the path difference is an integer number plus a half of the wavelength. For a single wavelength the variation of the intinsity versus the moving mirror position is a sine wave. For a broad band source there will be Fourier superposition of many waves resulting in an interferogram as shown in Fig. 3.10.

The resulting signal, called an interferogram carries information about every wave length in the IR range. When this beam is reflected by the sample certain wave

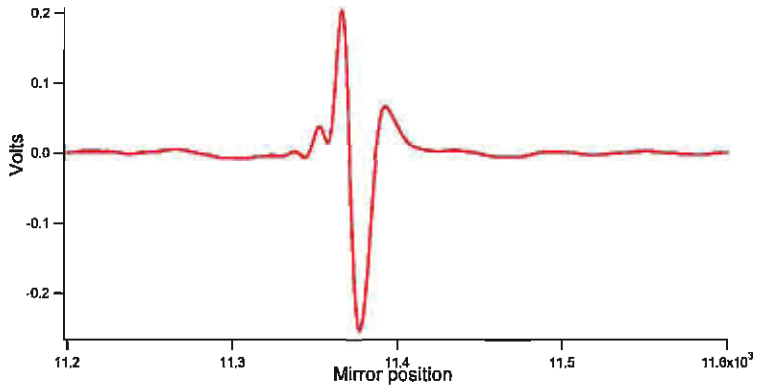

Figure 3.10: Example interferogram measured in the Bruker spectrometer in the mid infrared range.

numbers will be absorbed by the sample depending on its unique optical properties. Then, in reflectance measurement the reflected beam will be collected by a detector. The interferogram signal is digitized and sent to a computer where it can be decoded by a Fourier transform and generate the power spectrum (the intensity of light versus wavelength). An example is shown in Fig. 3.11.

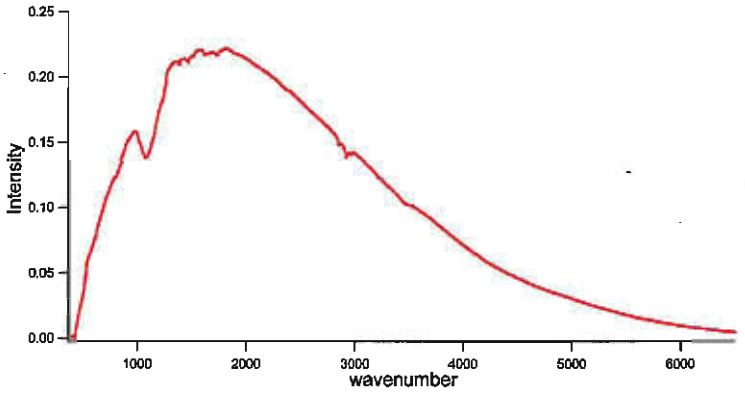

Figure 3.11: Example of a power spectrum in the mid infrared range.

3.2.2 Optical components

The spectrometer is designed to attach different components needed for each part of the spectra such as light sources in an easy way. The reflectance measurements were carried out in four separate ranges of frequency. A globar lamp was used as the light source of the far infrared and mid infrared ranges, and tungsten lamp for (NIR/VIS). For each spectral range, different optical components needed to be used to establish sufficient accuracy and sensitivity of the collected data. Table 3.1 summarize the combination of windows, beam splitters and the detectors used at each portion of the spectrum.

Range	Window	Beamsplitter	Detector
50 - 600 cm^{-1}	Polypropylene	6 μm Mylar with Ge	Bolometer 4.2 K
500 6000 cm^{-1}	KBr	Ge on KBr	MCT
5000 8000 cm^{-1}	KBr	CaF2	Ge diode
3000 12000 cm^{-1}	KBr	CaF2	MCT

Table 3.1: Optical components used in different portions of the spectrum.

3.2.3 The sample chamber

The sample chamber consists of three main parts: (i) the sample holder,(ii) the gold evaporating coils, and (iii) the cooling finger of the Janis Cryostat.

The head of the sample holder is designed as a two square faces perpendicular to each other made out of copper. The sample is mounted on one face and a reference mirror on the other face as it is shown in Fig. 3.13. To do temperature dependence measurement the sample side is connected to the cooling finger using silver foil. Silver is known by its high thermal conductivity among metals. Also thermal grease was

used to enhance the thermal contact between the silver and the sample holder. This allows reaching a lowest temperature of 23 K measured using a Si diode thermometer in close proximity to the sample. The sample holder is provided with a mechanical step rotator controlled by the computer to change between the sample and the reference during measurement at each temperature.

Figure 3.12: Sample holder

Figure 3.13: Sample holder head

At the beginning of each experiment the background spectrum was measured with the reference mirror and saved. During measurement detector and source drift are monitored using a reference mirror. At the beginning of the experiment the reference signal is divided by the background spectrum to produce the 100 % line (Fig. 3.14). The reference r_r and sample reflectance r_r are introduced as follows:

$$r_r = \frac{Reference}{Background} \tag{3.2}$$

And

$$r_s = \frac{Sample}{Background} \tag{3.3}$$

To eliminate the effect of the instrument and the environment as well as any possible mechanical distortion the reflectance of the sample r_s has to be divided by the reference reflectance r_r according to the following equation:

$$R_s = \frac{r_s}{r_r} \tag{3.4}$$

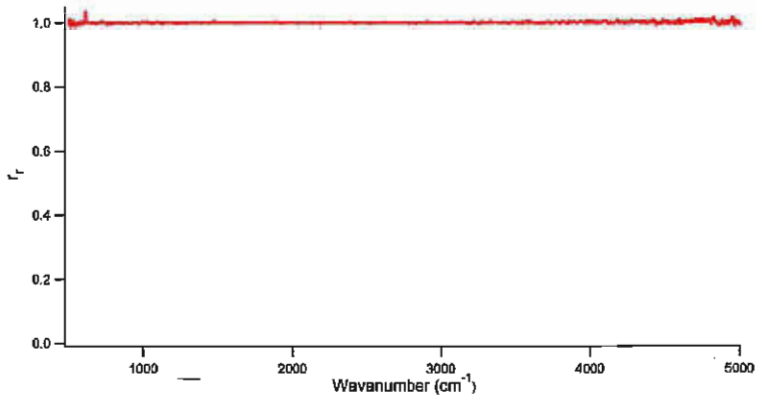

Figure 3.14: r_r at the begining of the experiment.

The gold evaporating coils are facing the sample holder head from one side so the sample can be rotated to face the coils. They are made of tungsten filaments and small pieces of gold have been attached to them. A power of about 25V × 2 Amp for 30 seconds was used to evaporate a thin layer of gold on top of the sample to eliminate any effect of the surface roughness of the sample on the optical reflectance. The gold coated sample reflectance is given by

$$r_{Au} = \frac{Gold/Sample}{Background} = r'_s \tag{3.5}$$

Therefore the actual reflectance of the gold coated sample is

$$R_{Au} = \frac{r_{Au}}{r'_r} = \frac{r'_s}{r'_r} \tag{3.6}$$

r'_r is the reference after gold evaporation. The absolute reflectance of the sample R_{abs} can then be achieved by the following equation:

$$R_{abs} = \frac{r_s}{r_r} \cdot \frac{r'_r}{r'_s} \tag{3.7}$$

If there were no lamp or detector drift then $\frac{r'_r}{r_r} = 1$

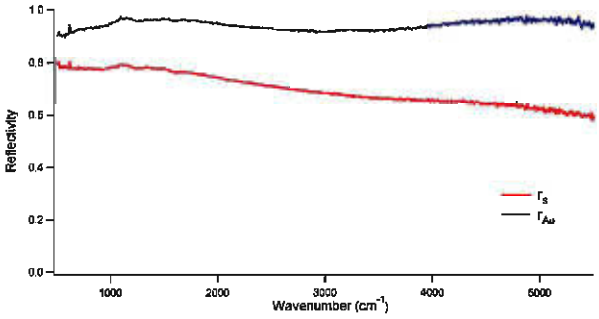

Figure 3.15: The reflectivity of the sample and the gold coated sample versus wavenumber.

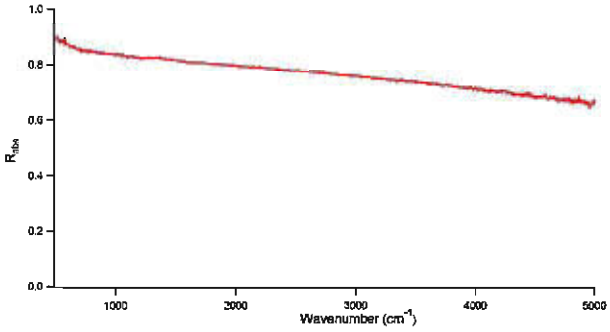

Figure 3.16: The Absolute reflectivity of the sample versus wavenumber.

Fig. 3.15 and Fig. 3.16 show the reflectance and the absolute reflectance of the sample respectively .

The cooling process of the sample is done by using liquid helium. The liquid helium flows through a rigid tube (cooling finger) to cool it down to 4.2 K. The helium boils off the end of the tube and because of the thermal gradient at the end of the cooling finger and the sample, liquid helium was able to cool the sample down to a limit of 23K.

Chapter 4

Results and discussion

4.1 Reflectance

4.1.1 Gadolinium (III) Oxide

The reflectivity of the cubic crytal structure Gd_2O_3 sample was measured in the spectral range 50 cm^{-1}-10000 cm^{-1}. Fig. 4.1 shows the reflectivity at room temperature and 23 K in the far infrared part of the spectrum. The extended range for room temperature is shown in Fig. 4.2.

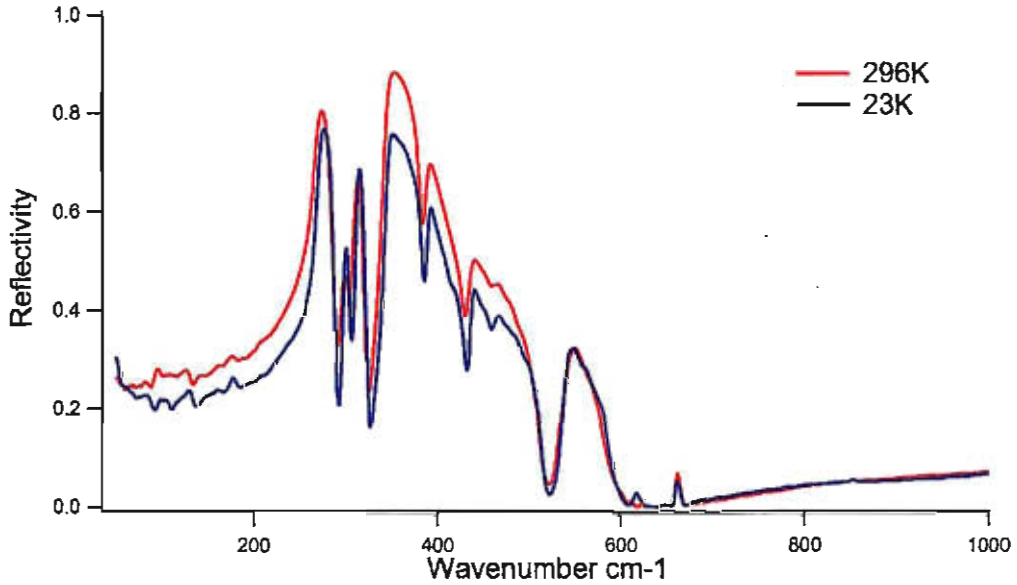

Figure 4.1: FIR reflectivity of Gd_2O_3 at temperatures 50 K and 296 K versus wavenumber.

From Fig. 4.2 it is observable that the sample has a typical insulator reflectivity with well defined phonons in the infrared range. The parameters of the Drude-Lorentz fit to the reflectivity (Fig. 4.3) are listed in table 4.1. The high frequency dielectric constant ϵ_∞ was estimated from the high frequency reflectivity using the Fresnel equation (Eq. 2.11) for a non-magnetic ($\mu = 1$) insulater with $\tilde{\epsilon} = \epsilon_\infty$ at high frequency.

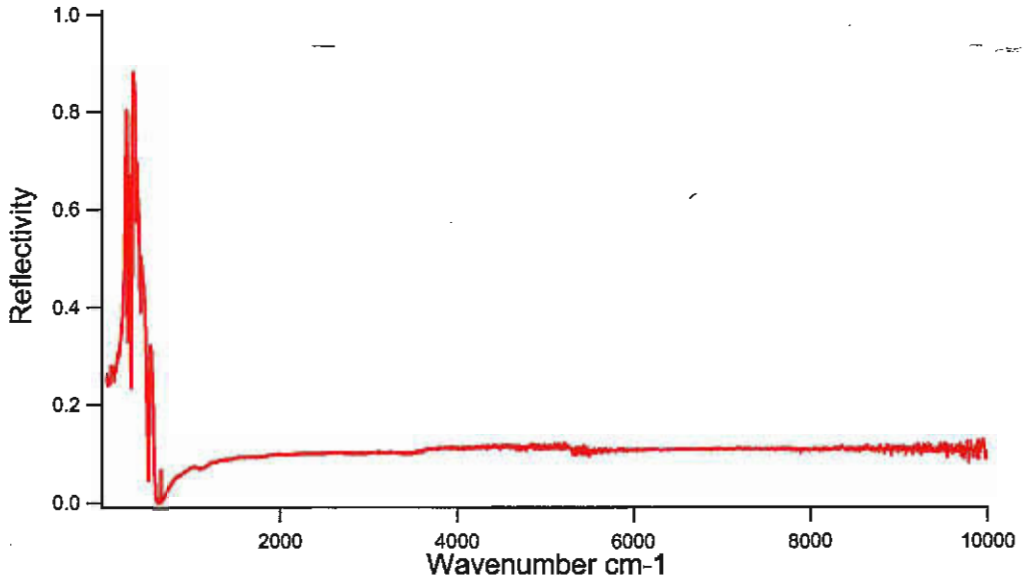

Figure 4.2: Gd_2O_3 reflectivity at 296 K versus wavenumber.

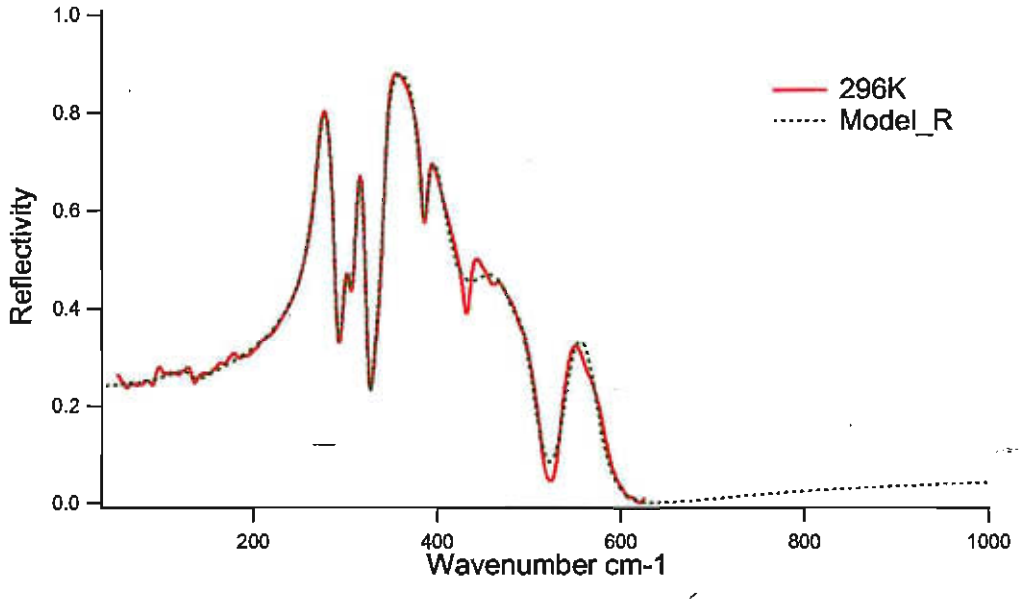

Figure 4.3: The experimental (from Fig. 4.1) and Drude-Lorentze model reflectivity of Gd_2O_3 at room temperature versus wavenumber.

4.1.2 Gadolinium

The temperature dependent reflectivity of the Gd sample for normal incidence in the spectral region between 50 cm^{-1} to 12000 cm^{-1} is shown in Fig. 4.4.

As it was explained in chapter 3, the measurements were taken in three different experiments. The data was adjusted by about ($\pm$ 0.01) and connected from different experiments in the overlap regions between them. The sample reflectance has been measured at four temperatures below the Curie temperature and at 296 K just above the Curie temperature. Note that below the Curie temperature the reflectivity for frequencies <2000 cm^{-1} increases as the temperature decreases. While near 4000 cm^{-1} the reflectivity decreases with temperature decreasing. The room temperature reflectivity behaves differently from the reflectivity of low temperatures, which means that this behaviour of the reflectivity is probably related to the magnetic ordering.

Oscillator number	$\omega_o \pm 0.5$ (cm^{-1})	$\omega_p \pm 50$ (cm^{-1})	$\Gamma \pm 5$ (cm^{-1})
1	130.5	60	22
2	269.6	450	8
3	299.9	200	12
4	310.9	220	7
5	343.3	380	7
6	386.7	110	12
7	433.5	270	82
8	484.1	40	24
9	538.5	150	26

ϵ_∞=3.89

Table 4.1: The Drude-Lorentz model parameters (Eq. 2.24 and Eq. 2.25) of Gd_2O_3 at 296 K in FIR.

As seen in Fig.4.5 the reflectivity from this work and that from Weaver [27] at 4.2 K for a single crystal shows a reasonable agreement in the overall shape.

4.1.3 The Effect of the Oxide Layer on Gadolinium Reflectivity

The reflectivity of Gd_2O_3 has been modeled using the RefFit software ([39]) to examine the influence of the oxide layer on the reflectivity of the Gd sample. As can be obtained from Eq.3.1, the estimated thickness of the oxide layer on the gadolinium sample that was used in this work is less than 6 nm. To explore the influence of the oxide layer on the reflectance of Gd, the experimental data was predicted using a two- layer model, (section 2.3.4 [39]). The inputs to the program are the dielectric

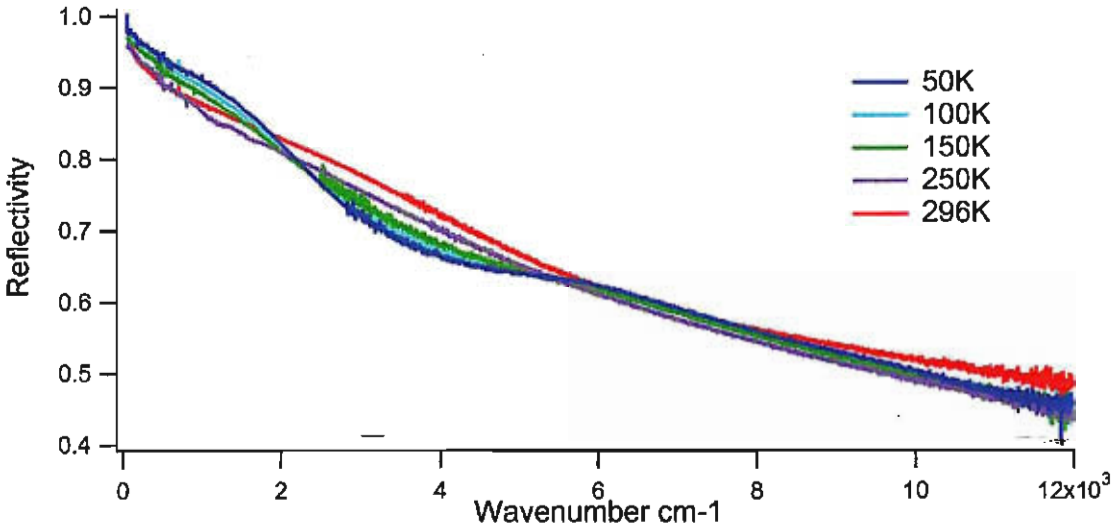

Figure 4.4: The experimental reflectivity of the Gd single crystal versus wavenumber at various temperatures.

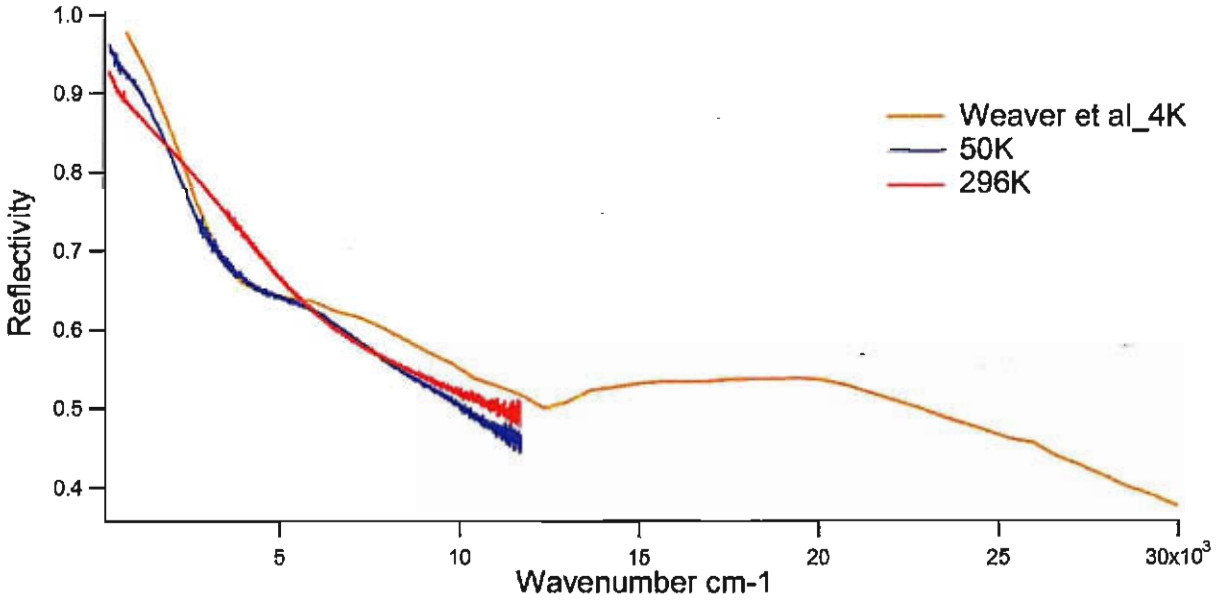

Figure 4.5: The experimental reflectivity of Gd at 50 K and 296 K (this work) and the data at 4.2 K from Weaver [27] versus wavenumber.

functions and the thicknesses of the layers. The dielectric function of a polycrystalline layer of Gd_2O_3 was determined from the measured R(ω) shown in Fig. 4.1 and Fig. 4.2 using a Drude Lorentz fit (Eq.2.30), while the metal under layer was considered to be a single Drude metal of (ω_p =28102 cm^{-1}, Γ=1805.5 cm^{-1}). These parameters give $\sigma(\omega=0)$ equal to the *dc* conductivity of Gd. Fig.4.6 shows the resulting reflectivity in the FIR. It is evident from Fig 4.6 that the existence of the oxide layer

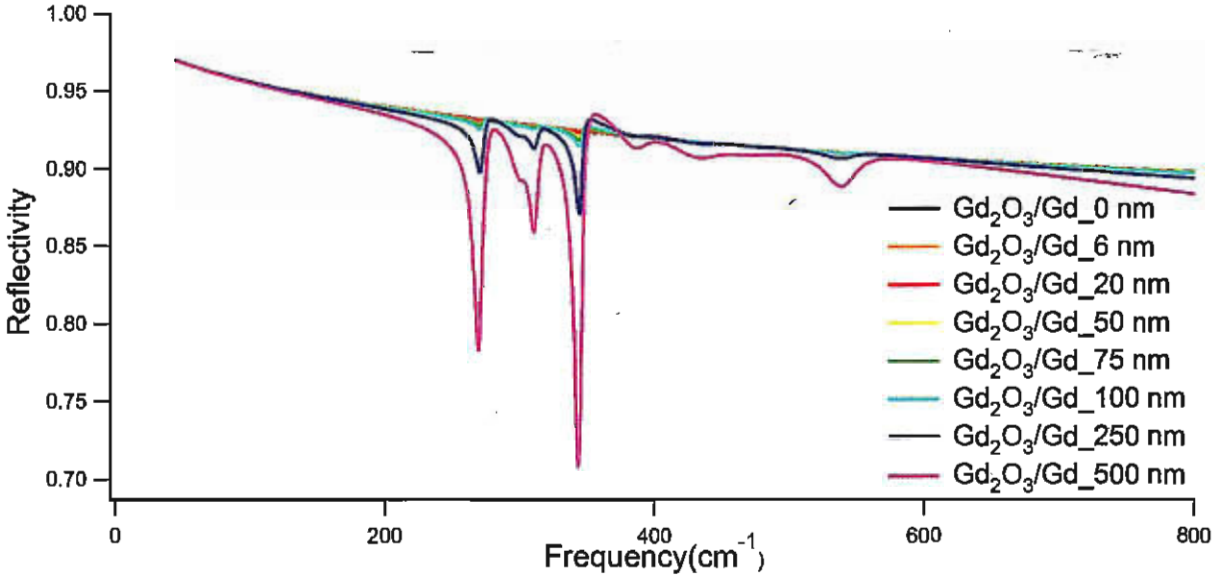

Figure 4.6: Modeled reflectivity of a Gd Drude metal with various thicknesses of Gd_2O_3 layer versus wavenumber in the FIR region.

does not have a big effect on the reflectivity for thicknesses less than 50 nm and for frequency range 0- 800 cm^{-1} . However, the reflectivity in the mid infrared frequency regime and higher seems to be affected strongly by the oxide layer. Fig. 4.7 is a plot of the reflectivity in the mid infrared with various oxide layer thicknesses. One can conclude that the influence of any Gd_2O_3 layer is negligible in the 0-8000 cm^{-1} frequency range. Note that the dip at 4000 cm^{-1} for the 250 nm thick layer is due to interference.

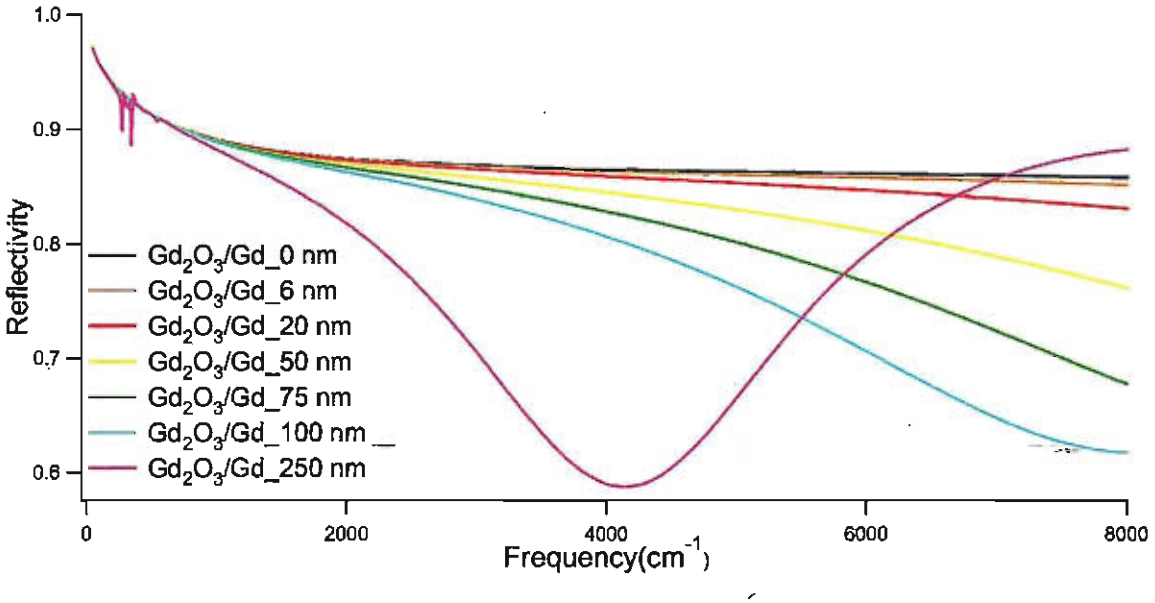

Figure 4.7: Modeled reflectivity of a Gd Drude metal with various thicknesses of Gd_2O_3 layer in the MIR region.

4.2 Optical Conductivity

Since the measurement of this work covers a limited range of the spectrum, the Kramers Kronig relations must be used to extract the optical response functions from the reflectivity data. This requires extrapolation of data to higher and lower frequencies. This work presents two approaches to extrapolate the data to high frequency depending on using the available data from previous work on Gd. Section 4.2.2 gives the two methods in detail. These high frequency extrapolations were utilized in order to get a sense of uncertainty in optical conductivity in the measured range (100 - 12000 cm^{-1}).

4.2.1 Low frequency extrapolation

For the low frequency extrapolation the Hagen-Rubens formula, Eq.2.31, was applied. The temperature dependent electrical resistivity of gadolinium single crystal was given

in [8]. Since the incident electromagnetic beam is parallel to the c-axes, the driven electrons moves parallel to the basal axis. The electric conductivity values along b-axes are given in table 4.2. From Fig 4.8 it is clear that the low frequency experimental

$T(K)$	$\rho - \rho_{res}(\mu\Omega.cm)$
50	16
100	45
150	70
250	119
296	132

b-axis $\rho_{res} = 4.9(\mu\Omega.cm)$

Table 4.2: The electrical resistivity of Gd single crystal [8]

reflectivity of this work is in good agreement with the Hagen-Rubens reflectivity for all temperatures.

4.2.2 High frequency extrapolation

The inconsistency of the high frequency data from different researchers introduces a difficulty in the high frequency extrapolation. Another difficulty is the lack of temperature dependent data. For instance, the reflectivity data of a single crystal from Weaver *et al.* at 4.2 K (Fig. 1.17) have shown a peak about 20000 cm^{-1}. This peak was not observed in Blodgett's reflectivity (Fig. 1.18) which was taken for an evaporated polycrystalline film at room temperature. Because of the uncertainty, two methods have been used to extrapolate the experimental data from this work to higher frequencies.

The first method is based on available reflectivity data from Weaver *et al.* [27]

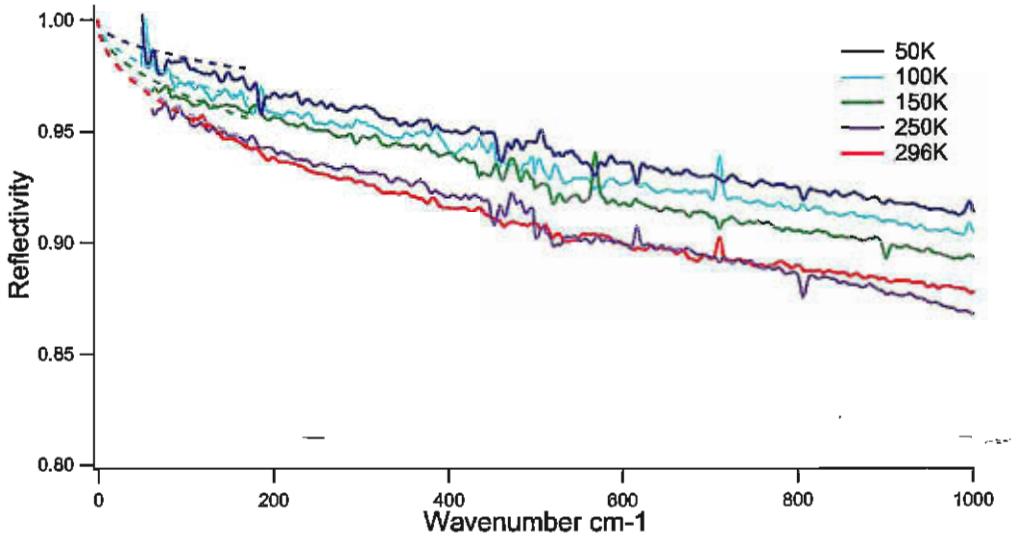

Figure 4.8: The experimental reflectivity of Gd (solid line) compared to Hagen-Rubens model reflectivity (dashed line) with ρ taken from table 4.2.

and Blodgett's data [28]. This approach assumed no temperature dependence of the features from both sources. Fig. 4.9 shows the reflectivity used for extrapolation up to 90000 cm^{-1}. The arrows in the graph indicates the frequency where Weaver's data was connected to the present work data at $\approx$ 12,000 cm^{-1} and the joint point between Weaver's and Blodgett's data was at $\approx$ 22,000 cm^{-1} . Note that about 4% have been subtracted from Blodgett's data to match up with Weaver's data. This approch will be referred as method I when the optical conductivity will be discussed in the next section.

The second method used in the extrapolation to higher frequencies assumed that the feature in Weaver's reflectivity has temperature dependence. This may or may not be true. This assumption was made only to get a sense of uncertainty in $\sigma_1(\omega)$. By examining the curve in Fig. 4.5 it is noticeable that there is a broad peak centered at 20,000 cm^{-1}. Since this data was taken at 4.2 K the second approach assumed that this feature to be related to the magnetic ordering. Therefore, it will be proportional

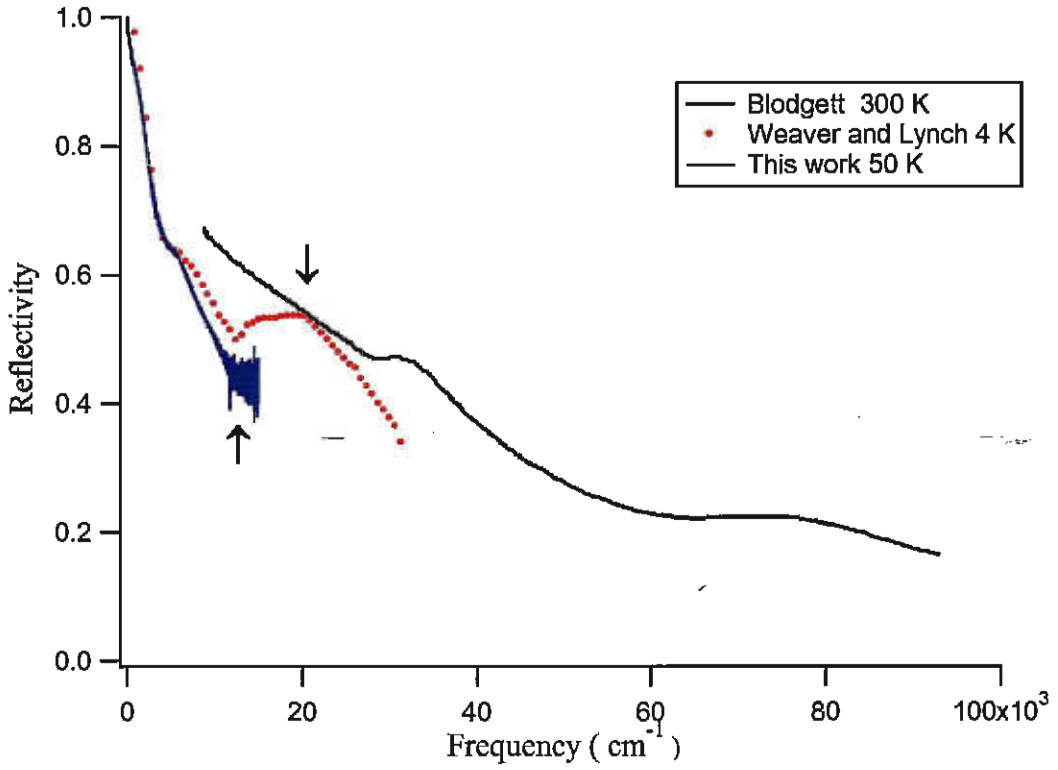

Figure 4.9: High frequency extrapolation method I, data from Weaver *et al.* [27] for a single crystalat 4.2 K and Blodgett for a polycrystalline sample at 300 K [28]. The arrows in the graph indicates the frequency where Weaver's data were connected to the present work data and Blodgett's data.

to the spontaneous magnetization of the sample. In order to use this data as a high frequency extrapolation to perform the K-K analysis a model reflectance was made for each temperature. Weaver's 4.2 K data were modeled by one Drude term and two Lorentz oscillators. The plasma frequency $\omega_p{}^2$ of one of the Lorentz oscillators which is related to the spectral weight was assumed to decrease as the temperature increases until it vanishes at room temperature. This assumption implies that $\omega_p{}^2 \ \alpha \ M_{(0,T)}$. The calculations have been done using the estimated ω_p for Weaver's data and the magnetization for single crystal Gd [8].

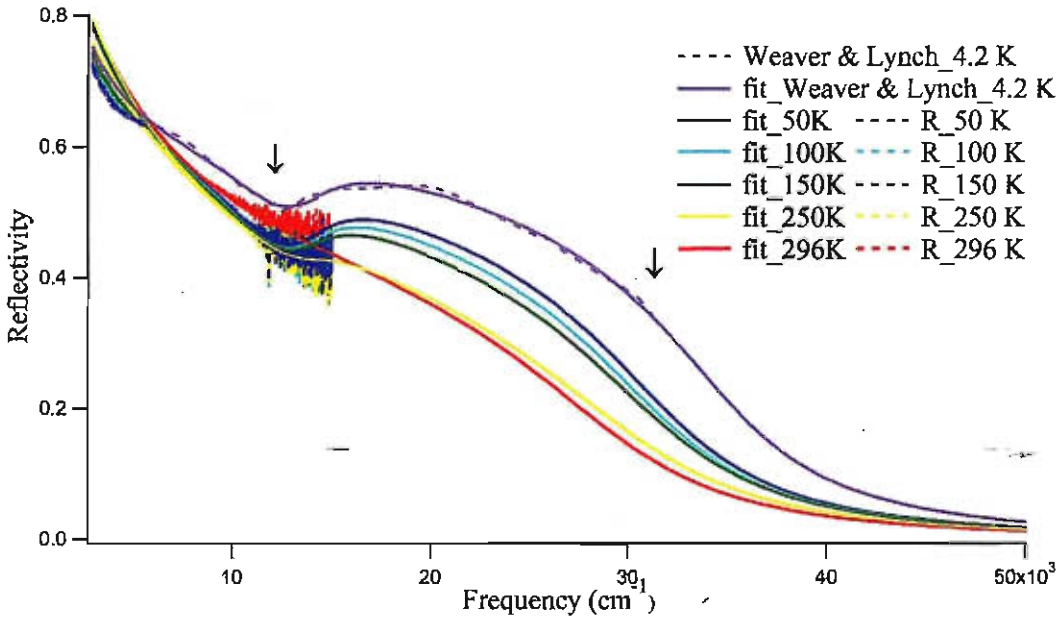

Figure 4.10: High frequency extrapolation method II. 4.2 K data from Weaver *et al.* [27]

Fig. 4.10 shows the resulted temperature dependence reflectivity which were used up to a limit of 30,000 cm^{-1} in the KK analysis. Note that ω_p for room temperature is set to be zero for the second oscillator. The Drude Lorentz fitting parameters for method II are given in Appendix A.

4.3 The effect of high frequency extrapolation on the optical conductivity

The two different high frequency extrapolations in this work resulted in a qualitatively similar Kramers - Kronig optical conductivity. A plot of the temperature dependence of the optical conductivity in the range 50-12,000 cm^{-1}, assuming Fig.4.9 high frequency extrapolation, is shown in Fig. 4.11. A similar plot of the optical conductivity

using method II (Fig. 4.10) of extrapolation to the high frequency is shown in Fig. 4.14. The real part of the optical conductivity has the same overall shape in both

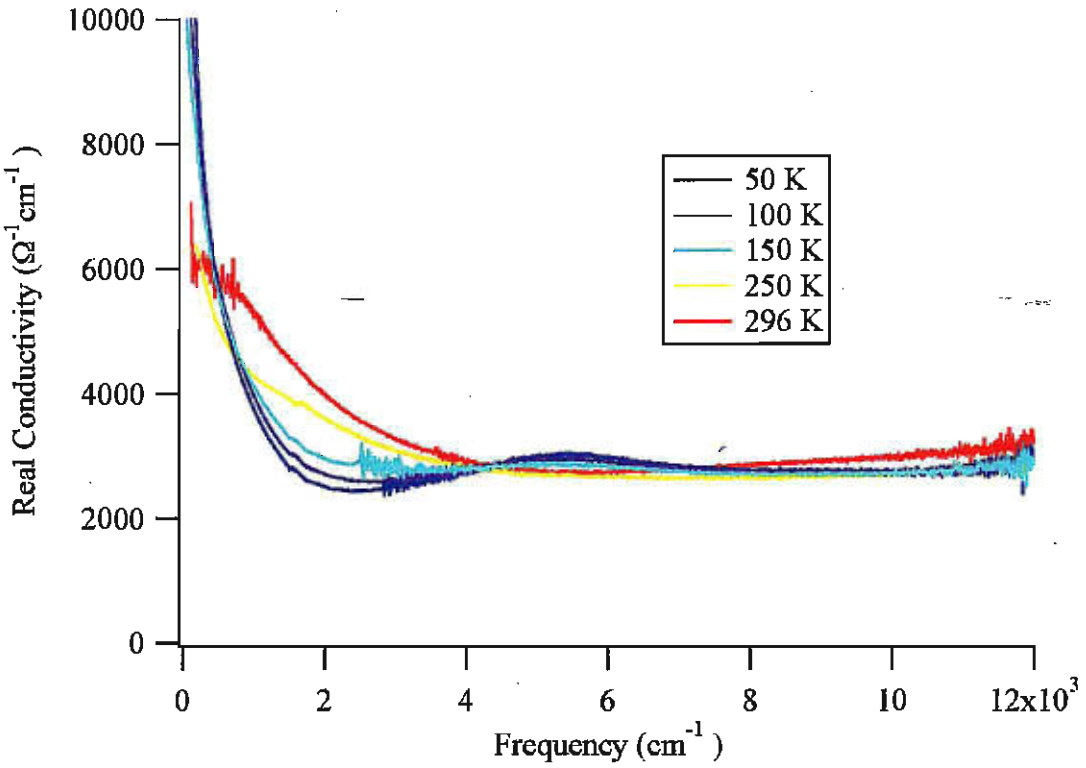

Figure 4.11: Real optical conductivity using method I of high frequency extrapolation versus frequency.

figures. They show the same feature around 5000 cm^{-1}. Although method I seems to give narrower feature. However, the two methods of extrapolation have shown a considerable difference in the absolute value of the optical conductivity. Applying method II has lowered the optical conductivity compared to that resulting from using method I (See Fig. 4.12 and Fig. 4.13). This can be understood from the sensitivity of KK analysis to the high frequency extrapolation. But, the absence of temperature dependent data in this range makes it difficult to determine which method is the best approximation. From this point on the optical properties resulted from using method

II will be presented.

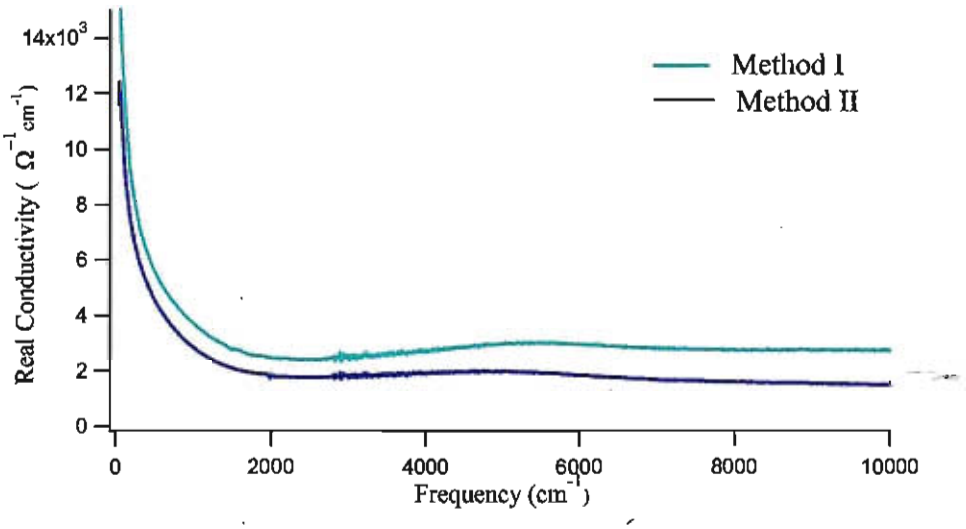

Figure 4.12: The optical conductivity at T= 50 K resulting from using method I and II high frequency extrapolation versus frequency.

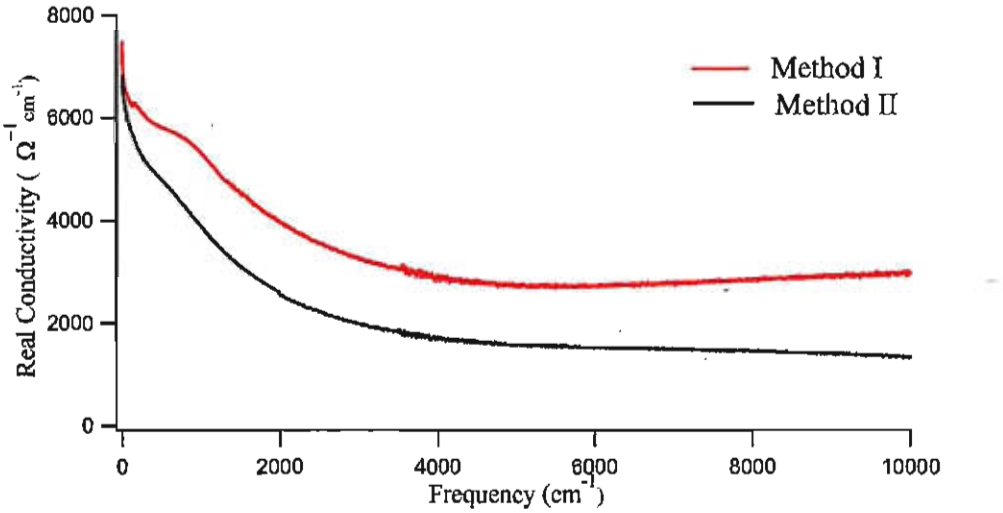

Figure 4.13: The optical conductivity at T= 296 K resulting from using method I and II high frequency extrapolation versus frequency.

Examining the resulting optical conductivity shows that the peak around 1.0 eV observed by Petrakian [31] and Hodgson [32] does not exist here. While the peak

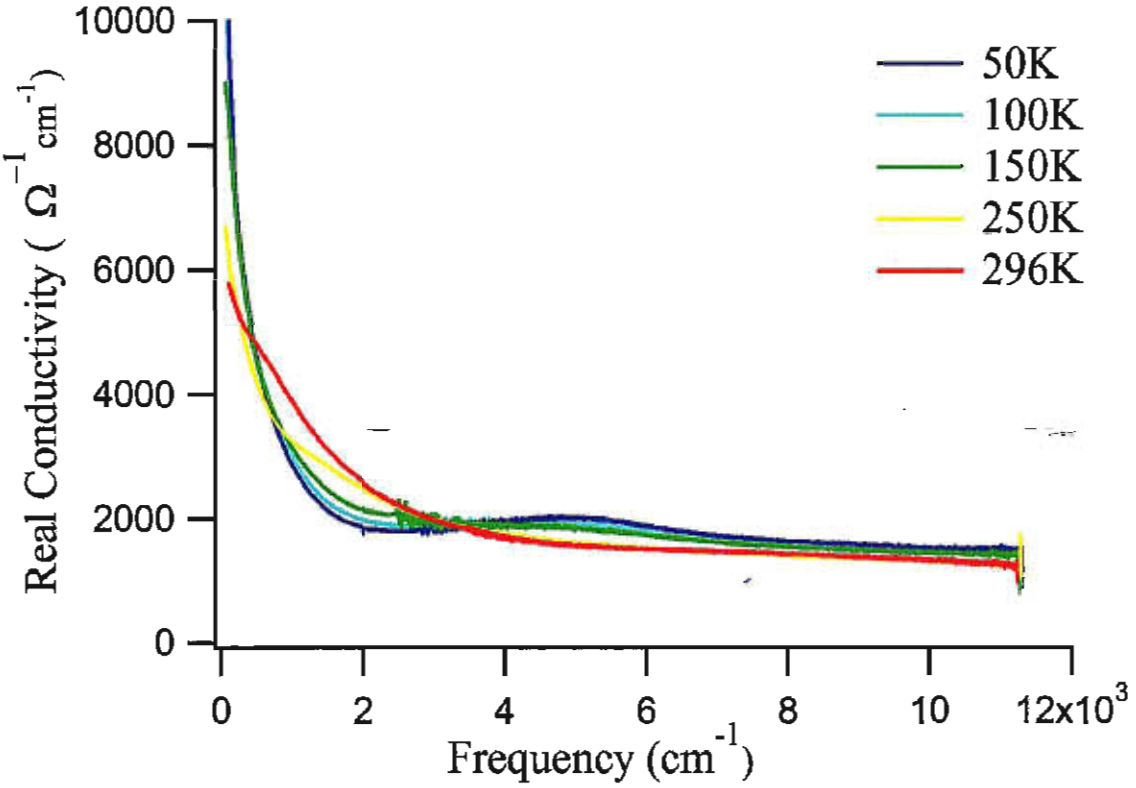

Figure 4.14: Real optical conductivity obtained from K-K analysis using method II for high frequency extrapolation versus frequency.

around 0.7 eV ,which is in good agreement among the different studies (see Table 1.2), is present in the ferromagnetic state. This is interesting because as has been discussed in section 4.1.3, the existence of the oxide layer affects strongly the optical data in the region of high frequency (> 8000 cm^{-1}). While the effect is weak particularly for thin layers (< 20 nm) in the low frequency region. Therefore, the discrepancy in the high frequency region could be partially attributed to the oxidation.

The optical conductivity also shows some agreement with the theoretical calculations by Victor Antonov [23]. The resulting optical conductivity from Antonov's band structure calculation using the Local Density Approximation (LDA) is shown in Fig. 4.15. In his calculation Antonov has considered the intraband transitions by

adding a Drude part to his calculations by hand (choosing Γ). The calculated optical conductivity at 0 K for spin polarized states along with the experimental optical conductivity from this work at 50K are shown in Fig. 4.15.

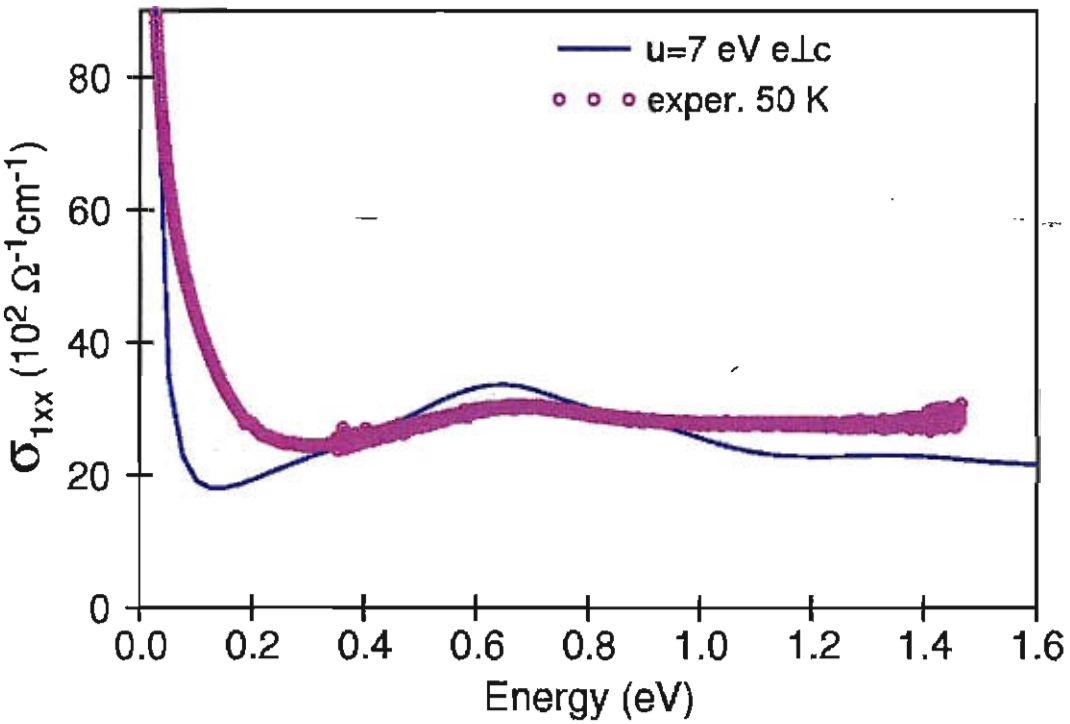

Figure 4.15: Real part of the optical conductivity [23]. The experimental data are from this work (method I).

It is clear that as a result of not including the intraband contribution in his calculations, Sapan's optical conductivity shows a drastic decrease in the energy range <1 eV (see Fig. 1.19). In contrast, Antonov's calculations were able to represent the structure at about 0.6 eV and the expected increase in the optical conductivity for a metal at low energy.

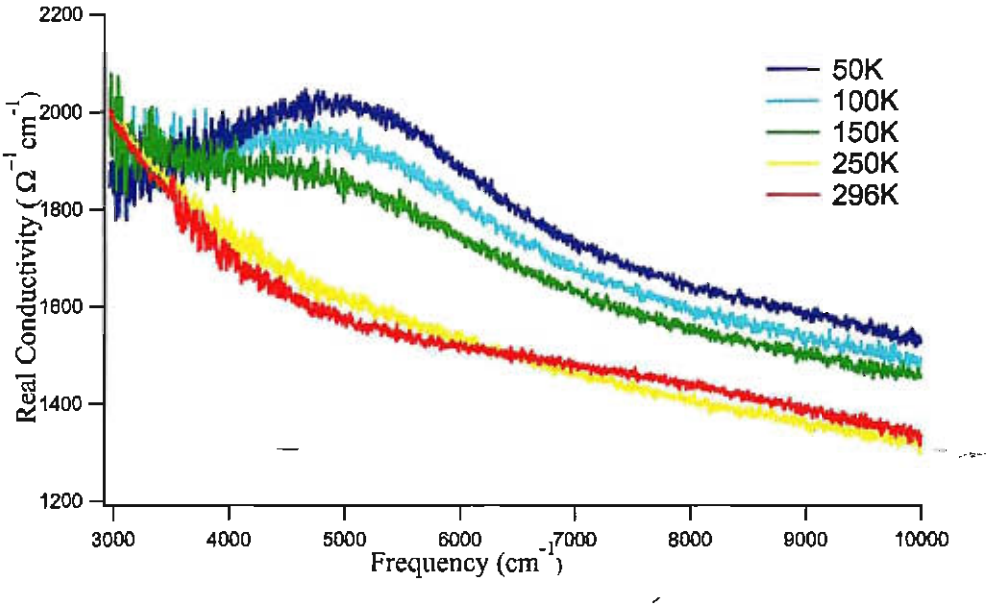

Figure 4.16: The peak in the real part of the optical conductivity (method II) at various temperatures versus frequency.

4.3.1 The Observation of Temperature Dependent Exchange Splitting

In this work a peak in the optical conductivity in the near infrared around 5000 cm^{-1} was observed. This feature is related to the exchange splitting of the $s-d$ conduction bands. The estimated ΔE of this interaction is $0.61eV$ [17]. Fig. 4.16 shows the temperature dependence of this peak. It should be noted that in the ferromagnetic state this peak decreases in magnitude as the temperature increases and it vanishes altogether at room temperature. Below T_c the centre of this broad peak shifts towards lower frequencies as the temperature increases. The calculations of Nolting *et al.* [13] supports this observation. Fig. 4.17 shows their resulting quasiparticle band structure of spin-up and spin-down electrons in the ferromagnetic state for three different temperatures. The lower two dispersions in Fig. 4.17 belong to the relatively broad s-like m_c=1,2 sub bands. It is clear from these graphs that the splitting decreases as

T increases and it collapses in the paramagnetic state [13]. Kim *et al.* [24] observed the same temperature dependence of the exchange splitting from the photoemission experiment on Gd single crystal (Fig. 4.18). Where in photoemission experiment the electromagnetic radiation incident on a solid excites the electrons from the ground state so some electrons can be detected outside the irradiated sample. The energy distribution curves (EDC) of the photoemitted electrons are recorded. Analysing the EDC reflects the energy dependence of the density of occupied electron states in the valence band [47].

From Fig. 4.18 it is noticeable that the peak in the intensity vs. binding energy is developing to two peaks as the temperature is lowered. Note that at temperatures higher than 0.7 T_c the two distinct peaks are no longer apparent [24]. But because the curve was a fitting of the T dependence of the binding energy assuming an equal spectral weights for the exchange splitting peaks, the composite peak continues to narrow until they merge at T_c [24]. This work observed the disappearance of the peak in the optical conductivity in the 250 K data which is about 0.85 T_c. Also, we should point out that this work gives much lower values for the exchange splitting compared to Kim's data. This can be explained by the fact that the exchange splitting is anisotropic in the reciprocal space. Note that Kim's measurement is along the Γ - A direction which is along the z-axis, while this work concerned about the basal axes in the directions Γ - M and Γ - K.

Observing the collapse of the exchange splitting near and above the Curie temperature is completely different from the behaviour found in the itinerant ferromagnetic systems such as Fe and Ni where there is still a finite exchange splitting persisting above T_c [24]. The observation in the optical conductivity is consistent with Kim's observation. Thus this work supports the fact that the mechanism of the ferromagnetism in Gd is more Stoner like than Hirsch's like. Hirsch's model suggests a change

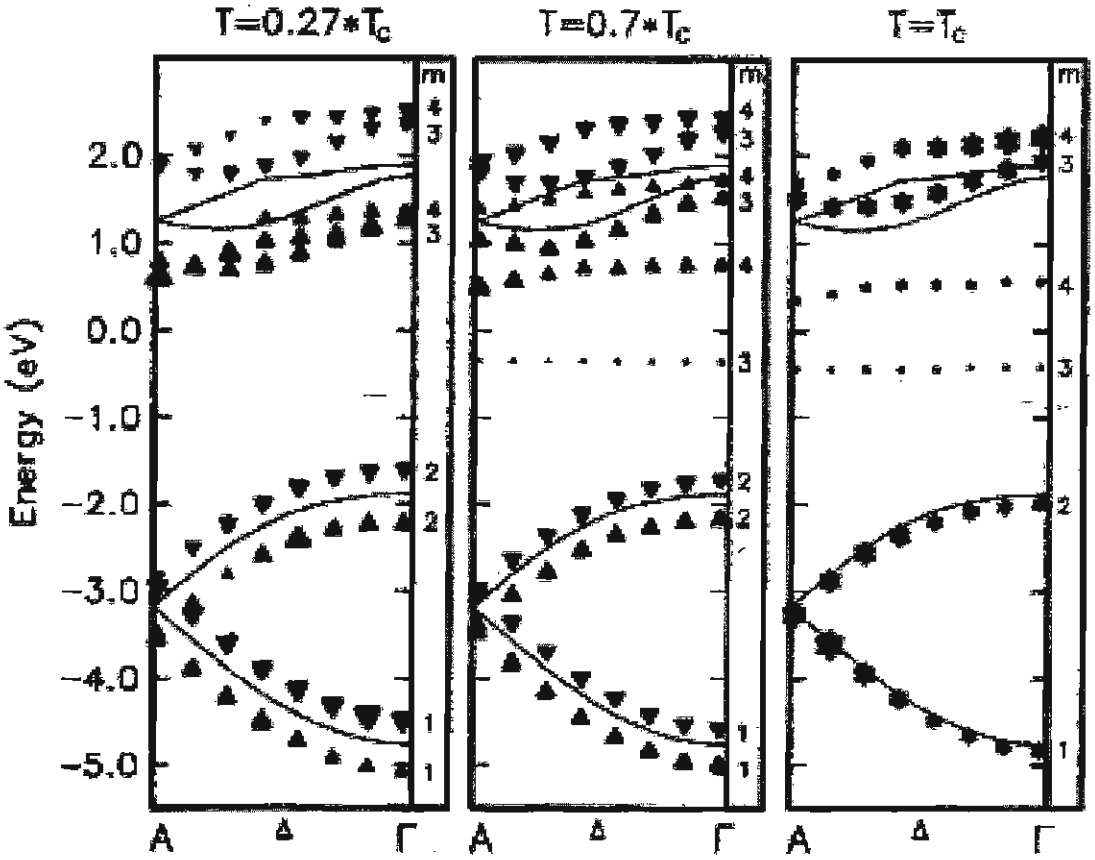

Figure 4.17: Quasiparticle energies in ferromagnetic Gd as functions of the wave-vector.The right columns present the index of the subband, to which the respective dispersion belongs. Triangles with top up (down) distinguish spin-up (spin-down)- dispersion. For T= T_c up and down dispersions coincide [13].

in the relative band width of the majority and minority spin electrons upon spin polarization. This mechanism should be seen as a transfer of the spectral weight (change in the effective mass) in optical absorption from high to low frequency upon spin polarization [4]. This signature of Hirsch's model is not observed in Gd optical data when integrating the optical conductivity between 100 and 3000 cm^{-1} according

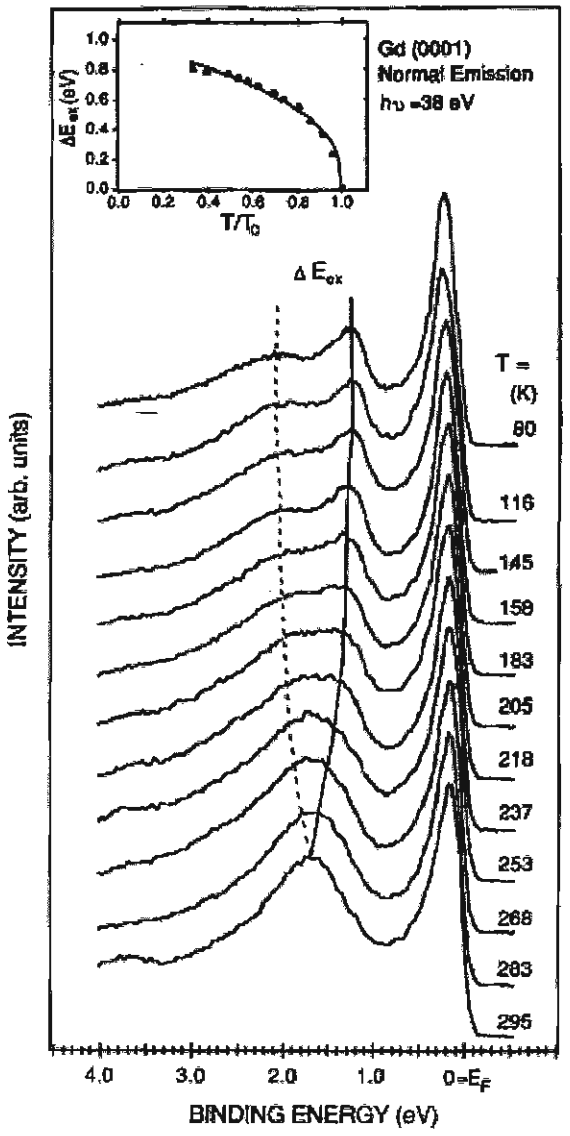

Figure 4.18: Temperature dependence of the exchange splitting for the Δ_2- spin up, and Δ_2- spin down energy bands between T =0.27 T_c and T= T_c at fixed $k_\perp$ for the photon energy $h\nu$=38 eV. Inset: Plot of the exchange splitting energy versus temperature obtained by experiment, and curve fitting using a power law of the form $\Delta E_{ex} = (1 - \frac{T}{T_c})^\beta$ [24].

to eq. 2.57 as will be discussed later.

4.4 The Effect of Smoothing Low Frequency Reflectance on K - K Conductivity

The low frequency optical conductivity generated using a low frequency extrapolation for two temperatures (50K and 296K) is presented in Fig.4.19. The far infrared reflectivity was fitted using a polynomial equation, and this curve used instead of FIR experimental data in the K-K analysis. This was to try to reduce noise in K-K transformation which tends to be large in the low frequency region. Note that the derived optical conductivity from the fitted reflectivity in the FIR lies on the average of the resulting conductivity from K-K calculations of the actual reflectivity. The same extrapolation was used to perform the KK in the frequency range 0-100 cm^{-1} using the Hagen - Rubens reflectivity. This was to get sense of the behaviour of the experimental optical conductivity as it approaches the zero frequency limit. It was found that the actual conductivity matches smoothly the resulting conductivity from HR reflectivity particularly at room temperature. However, real insight into the zero frequency limit of the optical conductivity awaits further measurements which cover the frequency range 0-100 cm^{-1}.

To explore the temperature dependence of the intraband scattering rate, the intraband conductivity has been separated from the interband contribution using the calculated interband conductivity by Antonov [23]. Fig. 4.20 shows the calculated interband optical conductivity by Antonov, Sapan [20], and the measured optical conductivity at 50 K and 296 K from this work (method I). Notice that the interband conductivity from the calculation of Sapan and Antonov are in good agreement. Also, it can be seen from Fig. 4.20, that in the frequency range (0 - 3000 cm^{-1}) the

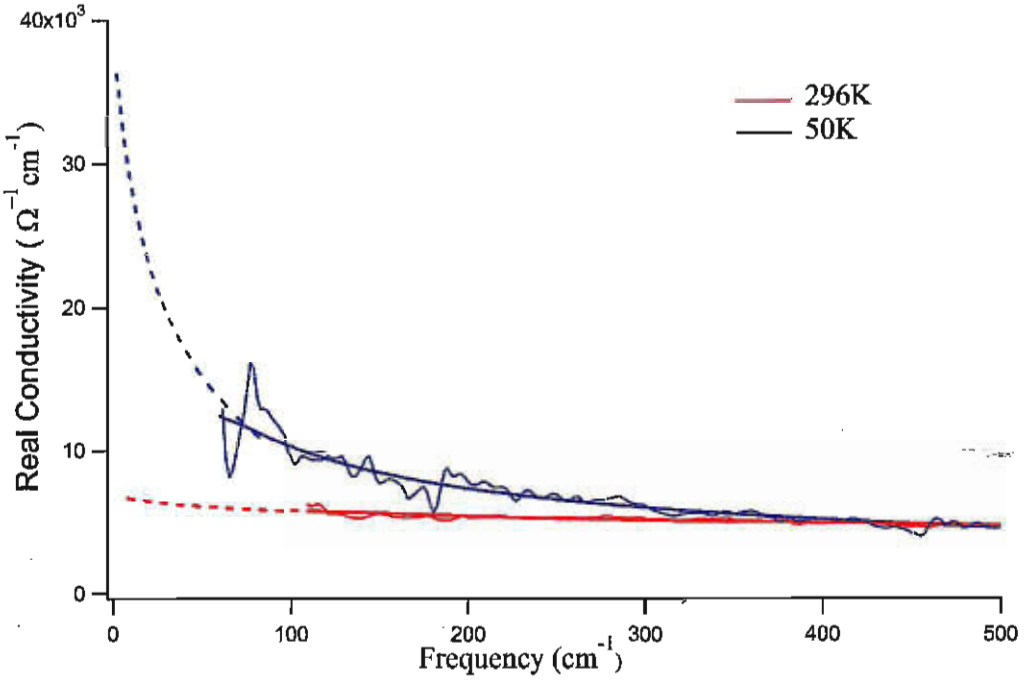

Figure 4.19: Real part of the optical conductivity in the far infrared range. The solid line represents the experimental and curve fitting of the conductivity (method II). The dashed line is the optical conductivity from the Hagen-Rubens extrapolations.

interband conductivity is well described by a linear approximation. Therefore, this part has been fitted to a linear approximation given by ($\sigma_{interband}(\omega) = 1000 + 0{:}5\omega$). Then, this part was subtracted from the measured optical conductivity to obtain the approximate intraband optical conductivity at the temperatures 50K, 100K and 150K. A constant background of 1000 Ω^{-1} cm^{-1}, has been subtracted, based on the zero frequency limit, from the measured optical conductivity at 250 K and 296 K. The reason is because the conductivity of these two temperatures does not show the feature around 5000 cm^{-1}. Furthermore, the flatness of the conductivity suggests a different manipulation to keep the consistency of the data.

With the only intraband conductivity, an estimation of the scattering rate has

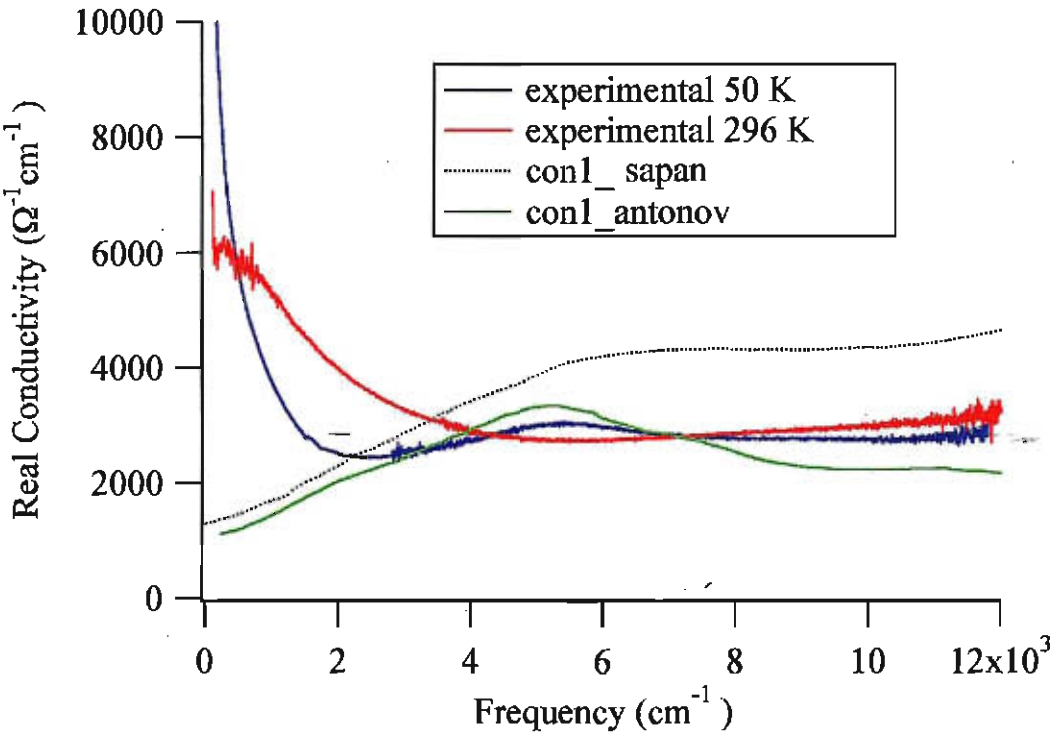

Figure 4.20: The calculated interband optical conductivity by Antonov [23] , Sapan [20], and the measured optical conductivity at 50 K and 296 K from this work (method I).

been made, where the scattering rate is defined as the width of the optical conductivity curve at $(\sigma_0/2)$. Therefore, the temperature dependent scattering rate was determined from the resulting experimental intraband conductivity curves at $(\sigma_0/2)$. The estimated values of the scattering rate at different temperatures are shown in Fig. 4.21 along with the electrical resistivity versus temperature. Note that the scattering rate decreases as the temperature decreases in the ferromagnetic state.

This can be well understood from the reduction in the spin disorder scattering of the conduction electrons as the magnetic spins become more ordered. Recalling that $(\rho \propto (\frac{m}{n})\Gamma)$ and comparing the temperature dependence of the scattering rate and the resistivity in Fig. 4.21, it is clear that, for temperatures in the ferromagnetic state,

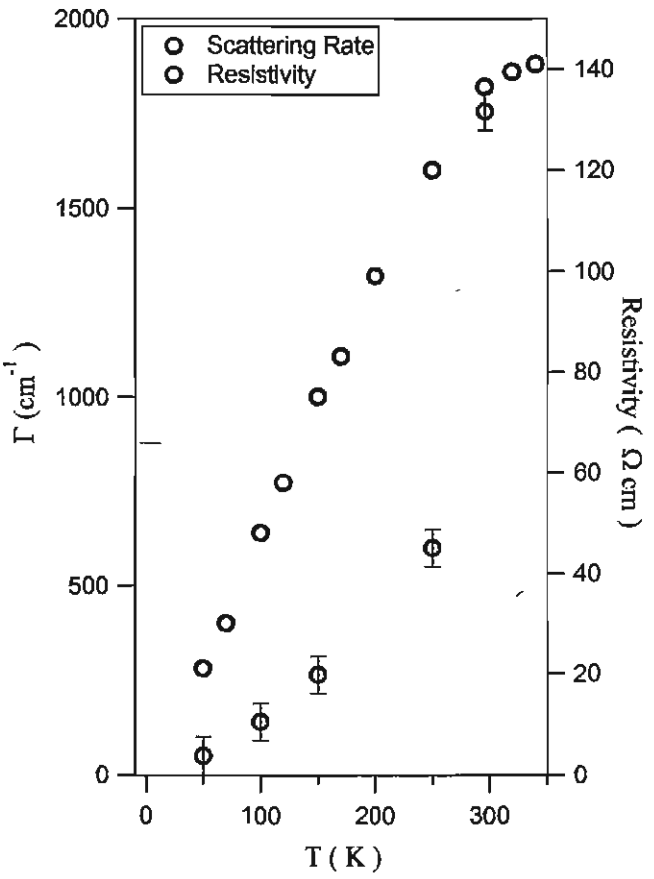

Figure 4.21: The scattering rate (left), and the resistivity of Gd single crystal [8] (right).

both ρ and Γ show a similar linear dependence on temperature, so it can be concluded that $\rho \propto \Gamma$ and the ratio $(\frac{m}{n})$ is either constant or n and m change simultaneously keeping this rate constant. However, the resulting scattering rate at T=296 K in the paramagnetic state shows a huge increase in contrast to the behaviour of the resistivity near and above the Curie temperature. This is interesting because it indicates that more than the spin disorder scattering is controlling the electrical resistivity as Gd enters the paramagnetic state.

The above observation in the behaviour of the scattering rate implies more investigation of the effective mass and the effective number of electrons. It is helpful to

examine the effective number of electrons using the partial sum rule. Basically the physical meaning of the sum rule is that any material at frequencies much higher than any of its responses, an electronic system responds to an electromagnetic perturbation in the same way as a system of an equal number of free electrons [48].

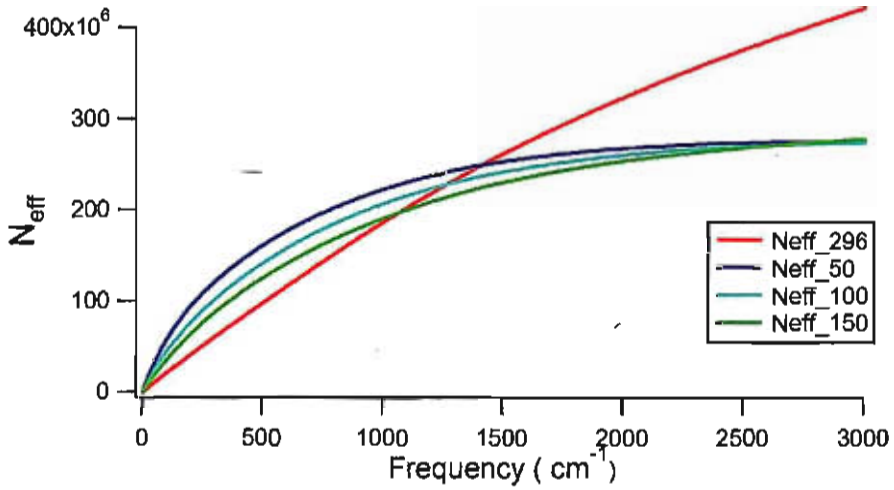

Figure 4.22: The effective number of electrons estimated from the experimental data using sum rule eq. 2.57 versus the upper limit of the integral.

Thus, the sum rule was employed in the present work to estimate the effective number of electrons contributing to the scattering process in the frequency range 0-3000 cm^{-1}. The optical conductivity used in the 0-100 cm^{-1} was the resulting conductivity from using HR reflectivity in K-K calculations. The resulting effective number of electrons versus frequency is shown if Fig. 4.22. Notice that the effective number of electrons is roughly constant for the temperatures 50 K, 100 K, 150 K. But there is a big change as the paramagnetic state is entered. This could suggest a change in the effective mass (recall Eq. 2.57) or it may also be due to a redistribution of the joint density of states.

Unfortunately, the complexity of the Hall effect particularly the difficulty of separating the OHC and the EHC, which strongly depend on the applied magnetic field

in a certain Hall measurement, prevents the generalization of the Hall coefficient behaviour of Gd single crystal and in turn prevents the determination of the temperature dependence of the concentration and the type of the current carriers.

Chapter 5

Conclusions

Temperature dependent optical reflectivity measurements have been conducted in the spectral range 100-11000 cm^{-1}, the lowest energy ever used to probe optical response functions of Gd single crystal. Also this work presents the same optical measuremenst, for the first time to our knowledge, for a bulk polycrystalline sample of Gd_2O_3, which has been used to explore the effect of the oxide layer on the optical reflectivity of Gd. Our analysis revealed the essential fact that the oxide layer, with thin thicknesses, has nearly no effect on the reflectivity of Gd in the low frequency range. In contrast the oxide layer has a big effect on reflectivity at high frequencies. This delivers a reasonable explanation for the discrepancy in the high frequency optical data of Gd in the literature.

K-K analysis was employed to extract the optical conductivity from the reflectivity data. Two methods were used as a high frequency extrapolation in the K-K calculation. It was concluded that for our data the resulting optical conductivity absolute value was sensitive to the method used. But both methods delivered the same overall shape and features.

The optical conductivity found to exhibit a peak in the mid-infrared range. This peak is a result of the exchange splitting of the conduction bands. This peak was observed in the optical conductivity at 50K, 100K, 150K. While this peak was absent in the 296K data in the paramagnetic state and also it was not observed in the 250K data in ferromagnetic state. This observation is consistent with the photoemis-

sion data which showed that the splitting vanishes at 0.7 T_c. In addition, our data successfully show the temperature dependence of the exchange splitting.

Gd is considered as a prototype of the localized ferromagnetic systems. Therefore, studying the mechanism of its ferromagnetism origin is important. In the light of the present work, the Stoner model is more appropriate to explain the origin of the ferromagnetism in Gd than Hirsch's model.

Another interesting observation of this work is the huge increase in the scattering rate in the paramagnetic state. This suggests that the electrical resistivity of Gd must be controlled by more than just changes in the scattering process.

Unfortunately exploring the behaviour of the optical response functions at very low frequency was faced by the limitation of the measurement of this work at 100 cm^{-1}. So, further low temperature and frequency measurements are needed to make a good connection between the experimental and theoretical studies.

Appendix A

Fitting Parameters

The Drude Lorentz parameters for different temperatures used for the high frequency extrapolations Fig. 4.10, which have been used to perform Kramer - Kronig analysis of the reflectance data.

T		Drude	1^{st} oscillator	2^{nd} oscillator
4 k	ω_0 (cm^{-1})	0	3699.88	13627.9
	ω_p (cm^{-1})	15220.7	30108.8	8345.45
	γ (cm^{-1})	25.095	12094.3	5619.36
50k	ω_0 (cm^{-1})	0	3699.88	13627.9
	ω_p (cm^{-1})	15220.7	27121.2	8302.9
	γ (cm^{-1})	81.07	13982.1	5619.36
100k	ω_0 (cm^{-1})	0	3699.88	13627.9
	ω_p (cm^{-1})	15220.7	27016.4	8044.77
	γ (cm^{-1})	208.483	14531.9	5619.36
150k	ω_0 (cm^{-1})	0	3699.88	13627.9
	ω_p (cm^{-1})	15220.7	27188.2	7732.67
	γ (cm^{-1})	324.307	15224.2	5619.36
250k	ω_0 (cm^{-1})	0	3699.88	13627.9
	ω_p (cm^{-1})	15220.7	27000.0	3869.03
	γ (cm^{-1})	478.74	17750.0	5619.36
296k	ω_0 (cm^{-1})	0	3699.88	13627.9
	ω_p (cm^{-1})	15220.7	26250	0
	γ (cm^{-1})	528.93	16800.0	5392.78

Table A.1: Drude and Drude-Lorentz parameters at different temperatures used to generate model II high frequency extrapolations.

Bibliography

[1] Yu. V. Knyazev and M. M. Noskov, " The Optical Properties of Rare Erth Metals," Phys. stat. sol. (b), **80**, 11 (1977).

[2] K. Maiti, M. C. Malagoli, E. Magnano, A. Dallmeyer, and C. Carbone, " Electronic Band Structure of Gd: A Consistent Description," Phys. Rev. Lett, **86**, 2846 (2001).

[3] E. C. Stoner, " Collective Electron Ferromagnetism ", Proc. R. Soc. London, Ser. A , **165**, 372 (1938).

[4] J. E. Hirsch, " Metallic Ferromagnetism without Exchange Splitting" Phys. Rev. B , **59**, 6256,(1999).

[5] L. Degiorgi, E. Felder, H. R. Ott, J. L. Sarrao, and Z. Fisk, " Low-Temperature Anomalies and Ferromagnetism of EuB_6 " Phys. Rev. Lett. , **79**, 5134,(1997).

[6] Karl A. Gschneidner, Jr. and Le Roy Eyring, *Handbook On the Physics And Chemistry Of Rare Earths Volume 1- Metals*, (Amsterdam: North-Holland ; New York, NY, USA : sole distributors for the U.S.A. and Canada, Elsevier North-Holland, 1978).

[7] David W. Snoke, *Solid State Physics : Essential Concepts*, (San Francisco : Paerson Education, Inc., 2009).

[8] H. N. Nigh, S. Legvold, and F. H. Spedding, " Magnetization And Electrical Resistivity Of Gadolinium Single Crystal" Phys. Rev, **132**, 1092,(1963).

[9] R. V. Colvin, S. Legvold, and F. H. Spedding, " Electrical Resistivity Of Heavy Rare-Earth Metals" Phys. Rev, **120**, 741,(1960).

[10] R. S. Lee AND S. Legvold, " Hall Effect of Gadolinium, Lutetium, and Yttrium Single Crystals" Phys. Rev., **162**, 431,(1967)

[11] S. A. Baily and M. B. Salamon, " Berry-Phase Contribution to the Anomalous Hall Effect in Gadolinium", Phys. Rev. B, **71**, 104407,(2005).

[12] Soshin Chikazumi, *Physics Of Ferromagnetism*, (2009, Oxford ; New York : Oxford University Press).

[13] W. Nolting, T. Dambeck, G Borstel, " Temperature-Dependent Electronic Structure Of Gadolinium", Z. Phys. B, **94**, 409,(1994).

[14] Roeland, L. W., Cock G. J., Jones, F. A., Moleman, A. C. McEwen, K. A., Jordan, R. G.,and Jones, D. W., " Conduction Electron Polarization of Gadolinium Metal", J. Phys. F: Metal Physics, **F5**, L233, (1975).

[15] Yu. S. Ponsov and G. A. Bolotin, " Influence Of Magnetic Ordering On Optical Phonons In Gd And Tb Single Crystal", Physics of the Solid State, **35**, 1437, (1993)

[16] K. N. Tayler and M. I. Darby, *Physics Of rare earth solids*, (1972, London: Chapman and Hall).

[17] J. O. Demmock, A. J. Freeman, R. E. Watson, " Electronic Band Structure and Optical Properties of Rare - Earth Metals", pp 237-45, *Optical properties and*

electronic structure of metals and alloys, Ed. F. Abeles, (Amsterdam: North Holland, 1966).

[18] Edward D. Palik, *Handbook of Optical Constants of Solids*, (Boston: Academic Press, INC., 1985).

[19] J K Lang, Y Baer, and P A Cox, " Study of the 4f and Valence Band Density of States in Rare-Earth Metals : II. Experiment and Results", J. Phys. F: Metal Phls., **11** , 121, (1981).

[20] Sapan Mohan, Nirpendra Singh, Tashi Nautiyal, and Sushil Auluck, " Optical and Magneto-Optical Properties of Gadolinium", J. Appl. Phys., **101**, 033523-1,(2007).

[21] B. N. Harmon and A. J. Freeman, " Spin-Polarized Energy-Band Structure, Conduction-Electron Polarization, Spin Densities, and the Neutron Magnetic Form Factor of Ferromagnetic Gadolinium", Phys. Rev. B, **10**, 1979,(1974).

[22] Dongqi Li, Jiandi Zhang, P. A. Dowben, and M. Onellion, " Temperature-Dependent Electronic Structure in a Localized-Magnetic-Moment System: Gadolinium", Phys. Rev. B, **45** , 7272,(1992).

[23] Victor Antonov, " private communication", Max-Planck-Institut for Solid State Research, Stuttgart, Germany.

[24] Bongsoo Kim, A. B. Andrews, J. L. Erskine, Kwang Joo Kim and B. N. Harmon, " Temperature-Dependent Conduction-Band Exchange Splitting in Ferromagnetic hcp Gadolinium: Theoretical Predictions and Photoemission Experiments", Phys. Rev. Lett., **68** , 1931, (1992).

[25] H. Miwa, " Energy Gaps and Electrical Resistivity Associated with Screw-Type Spin Arrangements", Prog. Theor. Phys., Japan, **29**, 477, (1963).

[26] C. Chr. Schuler, " Recent Studies on the Optical Properties of Rare-Earth Mwtals", pp 221-36, *Optical properties and electronic structure of metals and alloys*, Ed. F. Abeles, (Amsterdam: North Holland, 1966).

[27] J. H. Weaver and D. W. Lynch, " Anisotropic Optical Properties Of Heavy-Rare-Earth Single Crystals", Phys. Rev. Lett., **34**, 1324, (1975).

[28] A. J. Blodgett, W. E. Spicer and A. Y - C. Yu " The Band Structure of Gadolinium; Photoemission and Optical Studies", pp 246-56, *Optical properties and electronic structure of metals and alloys*, Ed. F. Abeles, (Amsterdam: North Holland, 1966).

[29] J. L. Erskine and E. A. Stern , " Magneto-Optic Kerr Effects in Gadolinium", Phys. Rev. B, **8**, 1239, (1973).

[30] Yu. V. Knyazev and G. A. Bolotin , " Influence Of Exchange Splitting On the Optical Properties Of Gadolinium And Dysprosium Single Crystals", Fiz. Metal. Metalloved., **58**, 1121, (1984).

[31] J. P. Petrakian, N Ahmed Mokhtar, and R. Fraisse , " Magneto-Optical Resonance In Ferromagnetic Gadolinium", Solid State communication, **24**, 397, (1977).

[32] J. N. Hodgson and B. Cleyet, " Absorption Bands of Gadolinium in The Ferromagnetic and Paramagnetic states", J. Phys. C, **2**, 97, (1969).

[33] Yu. V. Knyazev and M. M. Noskov, " Optical Properties of Gadolinium in the Infra-Red Renge of the Spectrum", Fiz. metal. metalloved., **32**, 1189, (1971).

[34] J. Krizek and K. N. R. Taylor, " Optical Properties of Rare Earth Films in Paramagnetic and Magnetically Ordered Phases", J. Phys. F: Metal Phys., **5**, 774, (1975).

[35] A Quemerais, B Loisel, G Jezequel, J Thomas and J C Lemonnier, " Optical Spectra of Gadolinium and Dysprosium: Study of the 5p Thresholds", J. Phys. F: Met. Phys., **11**, 293, (1981).

[36] Frederick Wooten, *Optical Properties of Solids*, (New York: Academic Press, INC., 1972).

[37] M. Fox, *Optical Properties of Solids*, (New York: Oxford university Press, 2001).

[38] O. S. Heavens, *Thin Film Physics* , (London: Methuen, 1970)

[39] Alexy Kuzmenko, *RefFit program*: http://Optics.unige.ch/alexy/reffit.html.

[40] Alexy Kuzmenko, *Guide to RefFIT software to fit optical spectra, Program version: 1.2.79*, (2009)

[41] PDF-card-Gd_2O_3-00-011-0604, International Centre for Diffraction Data (ICDD).

[42] PDF-card-Gd_2O_3-00-012-0474, International Centre for Diffraction Data (ICDD).

[43] PDF-card-Gd-00-002-0864, International Centre for Diffraction Data (ICDD).

[44] Alan K. Burnham and Glen T. Jerneson, " Oxidation Kinetics for Thin Rare-Earth Metal Films", J. Vac. Sci. Technol. A, **5**, 1713,(1987)

[45] *Bruker, IFS 66v/S User's Manual*, (1998).

[46] J. L. Erskine and C. P. Flynn, " Measurement of the 4*f*- Shell Optical Edge in Gd Metal", Phys. Rev. B, **14**, 2197, (1976).

[47] Wolfgang Schattke and Michel A. Van Hove (Eds.), *Solid-State Photoemission and Related Methods : Theory and Experiment* , (Weinheim : Cambridge : Wiley-VCH, 2002).

[48] M. Altarelli and D. Y. Smith , " Super Convergence and Sum Rules for the Optical Constants: Physical Meaning, Comparison with Experiment, and Generalization", Phys. Rev. B, **9**,1290, (1974)